

Assessment of zonal symmetric and asymmetric components of the Southern Annular Mode using a novel approach

Elio Campitelli * and Leandro B. Díaz

*Universidad de Buenos Aires, Facultad de Ciencias Exactas y Naturales, Departamento de
Ciencias de la Atmósfera y los Océanos, Buenos Aires, Argentina CONICET – Universidad de
Buenos Aires, Centro de Investigaciones del Mar y la Atmósfera (CIMA), Buenos Aires, Argentina
CNRS – IRD – CONICET – UBA, Instituto Franco-Argentino para el Estudio del Clima y sus
Impactos (UMI 3351 IFAECI), Buenos Aires, Argentina*

Carolina Vera

*Universidad de Buenos Aires, Facultad de Ciencias Exactas y Naturales, Departamento de
Ciencias de la Atmósfera y los Océanos, Buenos Aires, Argentina CONICET – Universidad de
Buenos Aires, Centro de Investigaciones del Mar y la Atmósfera (CIMA), Buenos Aires, Argentina
CNRS – IRD – CONICET – UBA, Instituto Franco-Argentino para el Estudio del Clima y sus
Impactos (UMI 3351 IFAECI), Buenos Aires, Argentina*

*Corresponding author: Elio Campitelli, elio.campitelli@cima.fcen.uba.ar

ABSTRACT

16 Enter the text of your abstract here. This is a sample American Meteorological Society (AMS)
17 \LaTeX template. This document provides authors with instructions on the use of the AMS \LaTeX tem-
18 plate. Authors should refer to the file `amspaper.tex` to review the actual \LaTeX code used to create
19 this document. The `template.tex` file should be modified by authors for their own manuscript.

20 *Significance statement.* This is significant because I wrote it.

21 **1. Introduction**

22 The Southern Annular Mode (SAM) is the main mode of variability in the Southern Hemisphere
23 extratropical circulation (Rogers and van Loon 1982) in daily, monthly, and decadal timescales
24 (Baldwin 2001; Fogt and Bromwich 2006) and exerts an important influence in weather conditions
25 such as temperature and precipitation anomalies and sea ice concentration (e.g. Fogt and Marshall
26 2020). Its positive phase is traditionally described as anomalously low pressures over Antarctica
27 surrounded by a ring of anomalous high pressures in middle-to-high latitudes.

28 Most authors describe the SAM as a zonally symmetric pattern, a fact that is reflected not only
29 in its name, but also in the various methods used to characterise it. Of the several different
30 indices presented in the literature, many of them are based on zonal means of sea level pressure or
31 geopotential height (Ho et al. 2012). Gong and Wang (1999) defined the SAM index as the zonal
32 mean sea level pressure difference between 40°S and 60°S, which is also the definition used by
33 the station-based index in Marshall (2003). Baldwin and Thompson (2009) proposed defining the
34 Northern and Annular modes as the leading EOF of the zonally averaged geopotential height at
35 each level.

36 Even though these indices are based on zonal averages, spatial anomalies of geopotential asso-
37 ciated with these indices (either by regression or composition) contain noticeable deviations from
38 zonal symmetry, particularly in the Pacific Ocean region. These zonal asymmetries have not been
39 widely studied, but previous work suggest that they strongly modulate the regional impacts of the
40 SAM (Fan 2007, Fogt et al. (2012), Rosso et al. (2018)), going as far as reversing its relationship
41 between precipitation in South America (Silvestri and Vera 2009). At the very least, the fact that

42 the SAM is not entirely zonally symmetric hinders our ability to reconstruct its historical variability
43 prior to the availability of dense observations in the Southern Hemisphere (Jones et al. 2009).

44 At least some of the variability associated with the zonal asymmetries of the SAM is probably
45 forced by the tropics. In particular, ENSO-like variability affects the Southern Hemisphere ex-
46 tratropics through the Pacific-South American Pattern (Mo and Ghil 1987; Kidson 1988; Karoly
47 1989), whose wave train projects strongly onto the zonal anomalies corresponding to the SAM
48 in the Pacific sector. And although the relationship between ENSO and SAM is far from simple,
49 tropical influences on the SAM have been observed (Fan 2007; Fogt et al. 2011; Clem and Fogt
50 2013). In particular, Fan (2007) computed SAM indices of the Western and the Eastern Hemi-
51 sphere separately and found that they were much more correlated if the (linear) signal of the ENSO
52 was removed. While this relates to temporally coherent variability of the two hemisphere and not
53 necessarily to zonal asymmetries in the associated spatial patterns, it is nonetheless consistent of
54 the ENSO playing a crucial role in zonal asymmetries of the SAM.

55 Positive trends in SAM index have been documented by various researchers using different
56 indices mostly on boreal Summer and Autumn (e.g. Fogt and Marshall 2020, and references
57 therein). These trends are thought of driven primarily by stratospheric ozone depletion and the
58 increase in greenhouse gases, and understood in the context of zonal mean variables (Marshall
59 et al. 2004; Gillett et al. 2005; Arblaster and Meehl 2006; Gillett et al. 2013). However, it's not
60 clear how or if the asymmetric component responds to this forcing, or whether its variability could
61 be masking influencing the observed trends independently.

62 Similarly unclear are the specific impacts of the zonally asymmetric component of the SAM.
63 Positive phase of the SAM is associated with generally colder temperatures over Antarctica and
64 warmer temperatures at higher latitudes (Jones et al. 2019) (and vice versa for negative SAM), but
65 there are significant deviations from this zonal mean response, notably in the Antarctic Peninsula

66 and the South Atlantic (Fogt et al. 2012). The SAM signal in precipitation behaves similarly,
67 although with even greater deviation from zonal symmetry (Lim et al. 2016). The importance of
68 zonal asymmetries of the SAM on these impacts have been studied in certain regions. For example,
69 the SAM-precipitation relationship in Southeastern South America and Southern Brazil can be
70 explained by the PSA-like zonally asymmetric circulation associated with the SAM (Silvestri and
71 Vera 2009; Rosso et al. 2018). Fan (2007) also found that precipitation in East Asia was impacted
72 by the variability of only the Western Hemisphere part of the SAM.

73 We are not aware of any previous work which quantifies the temporal variability of the asymmetric
74 component of the SAM with the exception of Fogt et al. (2012). However, their methods based
75 on composites of positive and negative SAM events leads to some issues, such as spatial patterns
76 derived from as little as 4 cases and from imbalanced periods (for example, 5 of the 7 cases in
77 their DJF SAM+ composite are from later than 1988, whereas all of the 8 years in their DJF SAM-
78 composite are from earlier than 1988). This is particularly important due to the inhomogeneities
79 in reanalysis products prior to the satellite era and the possible change in the asymmetric structure
80 of the SAM (Silvestri and Vera 2009). Moreover, Fogt et al. (2012) studied the zonal asymmetric
81 component of the SAM only in sea level pressure. Zonal asymmetries in the SAM spatial pattern
82 are fairly barotropic throughout the troposphere, but they change dramatically in the stratosphere
83 (Baldwin and Thompson 2009).

84 Our objective is, then, to systematically characterise the zonally asymmetric and symmetric
85 components of the SAM variability. For each level, we construct two indices which aim to capture
86 exclusively the variability of the symmetric and asymmetric component respectively. We assess
87 their vertical structure and coherence, temporal variability and trends. We then study the spatial
88 patterns described by the variability exclusive to each index. Finally, we investigate the relationship
89 of the SAM at 700 hPa with temperature and precipitation anomalies.

90 #LEAN: Te había hecho el comentario antes pero quizás no había sido del todo claro. Me parece
91 que acá hay que distinguir más en cómo se trabaja metodológicamente cada parte con respecto a
92 los niveles atmosféricos. Por ej. para la evaluación de los impactos solamente se está considerando
93 el índice troposférico.

94 In the Section 2 we describe the methods. In Section 3.a we describe the temporal variability
95 and vertical coherence of the indices. In Section 3.b, we analyse the spatial patterns of geopo-
96 tential height associated with them. In Section 3.c, we study their relationship with surface-level
97 temperature and precipitation.

98 **2. Methods**

sec:methods

99 **1) DATA**

100 To describe the Southern Annular Mode and its variability we used monthly geopotential height
101 at 2.5° longitude by 2.5° latitude of horizontal resolution and 37 vertical isobaric levels from ERA5
102 (Hersbach et al. 2020) for the period 1979 to 2018. We restrict our analysis to the post-satellite era
103 to avoid any confounding factors arising from the introduction of satellite observations.

104 To describe the relationship between the SAM indices and temperature and precipitation, we use
105 temperature data from NOAA's Merged Land Ocean Global Surface Temperature Analysis V4.0.1
106 (Smith et al. 2008; Vose et al. 2012), which blends land and ocean temperature analysis into a
107 monthly global grid 5° longitude by 5° latitude, and monthly rainfall 0.5° longitude by 0.5° latitude
108 data from the Global Precipitation Climatology Centre (Schneider et al. 2015, 2017). The rainfall
109 product uses station-based records, and thus it only has continental coverage.

2) DEFINITION OF INDICES

Traditionally the Souther Annular Mode (SAM) is defined as the leading Empirical Orthogonal Mode (EOF) of sea level pressure or geopotential height at lower levels (Ho et al. 2012). Following Baldwin and Dunkerton (2001), we extend that definition vertically and use the term SAM to refer to the leading EOF of the monthly anomalies of geopotential field south of 20°S at each level. We performed EOFs by computing the Singular Value Decomposition of the data matrix consisting in 481 rows and 4176 columns (144 points of longitude and 29 points of latitude). We weighted the values by the square root of the cosine of latitude to account for the non-equal area of each gridpoint (Chung and Nigam 1999).

To separate the zonally symmetric and asymmetric components of the SAM, we computed the zonal mean and anomalies of the full SAM spatial pattern, as shown in Figure 1 for 700 hPa. The full spatial signal ($\text{EOF}_1(\lambda, \phi)$) is the sum of the zonally asymmetric ($\text{EOF}_1^*(\lambda, \phi)$) and symmetric ($[\text{EOF}_1](\lambda, \phi)$) components. We then compute the “Full SAM”, “Asymmetric SAM” and “Symmetric SAM” indices as the regression coefficients of the regression of each monthly geopotential field on the respective patterns (weighting by the cosine of latitude). The three indices are normalized by dividing them by the standard deviation of the “Full” index at each level. As a result, the magnitudes between indices are comparable. However, only “Full” index will have unit standard deviation per definition. From the regression, we also use the explained variance of each pattern as an indicator of the degree of zonally symmetry or asymmetry of each monthly field.

Our method assumes linearity in the asymmetric component of the SAM. That means we assume that zonal symmetries associated with positive SAM are almost opposite and of the same magnitude to the ones associated with negative SAM. Fogt et al. (2012)’s composites (their Figure 4) suggest that this might not be entirely valid, although we argue that much of that apparent non-linearity

133 is due to the heterogenous nature of the selected years for constructing the composites. Using
134 our data (from 1979 to 2018), seasonal composites of zonal anomalies of geopotential height for
135 SAM+ (Full SAM index greater than 1 standard deviation) and SAM- (less than minus 1 standard
136 deviation) show relatively high pattern correlations for all seasons and are visually very linear
137 both for the troposphere (represented by the 700 hPa level) and the stratosphere (represented by
138 the 50 hPa level) (Figures A3 and A4). Therefore, we believe that our method is a reasonable
139 approximation of the phenomenon.

140 By computing a single EOF pattern using data for all months we are assuming that the zonal
141 anomalies of the SAM are the same in all seasons – December to February (DJF), March to May
142 (MAM), June to August (JJA) and September to November (SON). Geopotential zonal anomalies
143 computed by projecting the first EOF of each season independently are very similar to each other in
144 the troposphere (Figure A5, row 1) and show pattern correlations between 0.65 (DJF with JJA) and
145 0.9 (MAM with SON). In the stratosphere (Figure A5, row 2), patterns are similar for all trimesters
146 except DJF, when the wave-1 zonal anomalies are rotated 90° in comparison with the rest of the
147 year. Pattern correlations in the stratosphere are between -0.24 (DJF with SON) and 0.95 (MAM
148 with JJA). Based on this, we believe that our initial assumption is not unreasonable through most
149 of the year with the exception of DJF in the stratosphere.

150 Finally, we assume that the zonally asymmetric pattern is stationary in time. Silvestri and Vera
151 (2009) suggest that this might not be the case between 1958 and 2004 but the period we analyse is
152 much shorter (1979 – 2018) so it's unlikely that we could observe significant changes. Moreover,
153 zonal asymmetry of the spatial patterns for the two halves of the period (1979 to 1998 and 1999 to
154 2018) show no systematic change neither in the stratosphere nor in the troposphere (Figure A6).

3) REGRESSIONS

We perform linear regressions to quantify the association between the SAM indices and other variables. Since the Asymmetric and Symmetric SAM indices are significantly correlated with each other, to capture the variability explained uniquely by each index we use one multiple linear regression instead of two simple linear regressions. To obtain the linear coefficients of a variable X (geopotential, temperature, precipitation, etc. . .) with the Asymmetric SAM (SAM_a) and Symmetric SAM (SAM_s) we fit the equation

$$X(\lambda, \phi, t) = \alpha(\lambda, \phi)SAM_a + \beta(\lambda, \phi)SAM_s + X_0(\lambda, \phi) + \epsilon(\lambda, \phi, t)$$

where λ and ϕ are the longitude and latitude, t is the time, α and β are the linear regression coefficients, X_0 and ϵ are the constant and error terms. From this equation, α represents the (linear) association of X with the variability of the Asymmetric SAM that is not explained by the variability of the Symmetric SAM; i.e. it is proportional to the partial correlation of X and the Asymmetric SAM, controlling for the effect of the Symmetric SAM and vice versa for β . When performing a separate regression for each trimester (DJF, MAM, JJA, SON), we average the relevant variables seasonally for each year and trimester before computing the regression.

At 2.5° by 2.5° resolution, a single regression field is composed of thousands of regressions. In such case, using p-values to test for significance leads to misleading results (Walker 1914; Katz and Brown 1991). While there are multiple proposed solutions in the literature, Wilks (2016) suggests that adjusting p-values by controlling for the False Discovery Rate (Benjamini and Hochberg 1995) is a simple and effective method to ameliorate this issue. Therefore, p-values showed in regression fields are all adjusted following Benjamini and Hochberg (1995).

We computed linear trends by Ordinary Least Squares and the 95% confidence interval assuming a t-distribution of the appropriate residual degrees of freedom. To compute the amplitude of the zonal waves we computed the Fourier transform of the spatial field at each latitude circle.

We computed density probability estimates using a gaussian kernel of optimal bandwidth according to Sheather and Jones (1991).

4) COMPUTATION PROCEDURES

We performed all analysis in this paper using the R programming language (R Core Team 2020), using the data.table package (Dowle et al. 2020) and the metR package (Campitelli 2020). All graphics are made using ggplot2 (Wickham 2009). We downloaded data from ranalysis using the ecmwfr package (Hufkens et al. 2020) and indices of the ENSO with the rsoi package (Albers and Campitelli 2020). The paper was rendered using knitr and rmarkdown (Xie 2015; Allaire et al. 2019).

3. Results

sec:results

a. Temporal evolution

sec:temporal

We first asses the temporal evolution of the Asymmetric SAM and Symmetric SAM. Figure 2 shows the corresponding time series for 700 hPa and 50 hPa and their corresponding density estimates. We selected these two levels as representative of the tropospheric and stratospheric variability respectively. As will be shown later, both indices are highly coherent within each atmospheric layer, therefore is reasonable to take one level as representative of each layer.

Month-to-month variability is evident for both indices, with noisy variations in the low frequency. At first glance the series can be distinguished by their distributions. Compared to the tropospheric indices, the stratospheric indices are much more long-tailed; that is, extreme values (both negative

197 and positive) abound. The Asymmetric SAM series have both more variability in the higher
198 frequencies than the Symmetric SAM series.

199 The stratospheric Symmetric SAM varies strongly with a two-year period, which can be seen by
200 spectral analysis (Figure A2). This might suggest a link between stratospheric SAM variability
201 and the Quasi-Biennial Oscillation (Baldwin et al. 2001). There is a local peak at 2 years in the
202 periodogram of the tropospheric Symmetric SAM also, although it's not statistically significant. In
203 the troposphere the most significant peak of variability is found in the Asymmetric index at around
204 3.6 months.

205 From Figure 2 we can see that the Asymmetric SAM and Symmetric SAM time series appear
206 to be correlated. Moreover, looking at the extremes in the stratosphere, the Symmetric SAM
207 series appears to lag the Asymmetric SAM series (see, for example, the positive events on late
208 1987). We show these correlations, across all the levels of the reanalysis for zero and -1 lag
209 (Asymmetric SAM index leading the Symmetric SAM index), in Figure 3. Zero-lag correlations
210 between the Asymmetric SAM and Symmetric SAM series are relatively constant throughout
211 the troposphere, fluctuating between 0.39 and 0.45. One-month-lag correlations are similarly
212 constant but significantly reduced to around 0.17. In the stratosphere, zero-lag correlations drop
213 to a minimum of 0.21 at 20 hPa and then it increases again monotonically with height up to the
214 uppermost level of the reanalysis (although results near the top of the models are to be interpreted
215 with care). At the same time, one-month-lag correlations increase with height. As a consequence,
216 stratospheric Asymmetric SAM index tend to precede corresponding Symmetric SAM index.

217 Figure 4a shows (zero-lag) cross-correlation across levels for the Full, Symmetric and Asym-
218 metric SAM indices. For the Full SAM (panel a), high values below 100 hPa reflect the vertical
219 (zero-lag) coherency throughout the troposphere. Above 100 hPa correlation between levels falls
220 off more rapidly, indicating less coherent (zero-lag) variability. Therefore, there is a non negligible

correlation between the troposphere and the lower-to-middle stratosphere. Examining panels b and c, we see that the Asymmetric and Symmetric SAM share the same high level of coherency in the troposphere but they differ in their stratospheric behaviour. Stratospheric coherency is stronger for the Asymmetric SAM than the Symmetric SAM. The stratospheric Symmetric SAM seems to connect more strongly to the troposphere than the Asymmetric SAM.

The linear trends for each of the indices (Full SAM, Symmetric SAM and Asymmetric SAM) were evaluated for the complete period 1979 – 2018 at each level (Figure 5) for the whole year and separated by trimesters. The Full SAM index presents a statistically significant trend (panel a.1) that extends throughout the troposphere up to about 50 hPa and reaches its maximum value at 100 hPa. The seasonal trends (rest of column a) indicate that positive trends are present in Autumn and particularly in Summer, where the 100 hPa maximum is much more defined. In Winter and Spring, we detect no statistically significant trend. This is consistent with the results of previous studies, which find clear positive trends in Summer, weaker in Autumn and no trends in the other seasons (e.g. Fogt and Marshall 2020, and references therein) using indices of the SAM based on surface or near-surface circulation.

By separating the SAM signal in its asymmetric and symmetric parts, we can not only see that these trends are almost entirely due to the symmetric component (column b vs. column c), but in some cases the trends become more clear. In Summer, the Asymmetric SAM has a statistically non significant negative trend in the middle troposphere that obscures the trend in the Full SAM index; as a result, trends computed using only the Symmetric component are more clear (compare the shading region in panel a.2 and c.2). In Autumn, the Symmetric SAM reveals a statistically significant positive trend in the stratosphere that is not significant using the Full SAM index.

We stress that these are only linear trends during the whole period and the absence of a statistically significant signal should not be taken as evidence of no systematic change. In particular, going

back to Figure 2, we can see an evident change in the stratospheric Asymmetric component (red line in panel a) between the 90's, when we see a dominance of extreme negative values, and the 00's, when we see the inverse. This change is restricted to the Winter months: the linear trend for Winter starting in 1990 for the Asymmetric component at 50hPa is 0.37 ± 0.22 .

Figure 6 shows decadal trends for the explained variance of each index. There is no evidence of a significant trend in the stratosphere. In the troposphere, there is a positive trend for the Asymmetric SAM and not significant trend for the Symmetric SAM. This suggest that the SAM has become more asymmetric in the period from 1979 to 2018. However, the change is slight, around 1% increased explained variance per decade.

b. Spatial patterns

sec:spatial

To show if, and to what extent, the Asymmetric and Symmetric SAM indices indeed capture the asymmetric and symmetric component of the SAM respectively, we computed the spatial regression of geopotential height anomalies on these indices and the Full SAM index for 700 hPa and 50 hPa levels. Figure 7 shows these regressions. Regression coefficients in column a are computed using the Full SAM. Regression coefficients in columns b and c are computed using multiple regression using the Asymmetric and Symmetric indices at the same time. Thus, they are to be interpreted as the patterns associated with each index, removing the variability (linearly) explained by the other index.

In the stratosphere, the spatial pattern associated with the Full SAM is more clearly dominated by a zonally symmetric, monopolar structure (panel a.1) which is, however, not perfectly centred in the South Pole. The monopole obtained by the regression pattern for Symmetric SAM (panel c.1) is much more symmetric and the shift from total symmetry is captured by the regression pattern of

the Asymmetric SAM as a wave-1 with maximum anomalies above the Belinghausen Sea on the Western Hemisphere and Davis Sea in the Eastern Hemisphere (panel b.1).

In the troposphere, panel a.2 shows the well known combination of zonally symmetrical annular mode with zonal asymmetries in the form of a wave-3 (Fogt et al. 2012). The regression using the Asymmetric and Symmetric SAM indices successfully disentangle both structures. The Asymmetric SAM index gives rise to a cleaner zonal wave (panel b.2) and the Symmetric SAM index is associated with an annular mode, almost devoid of zonal asymmetries (panel c.2). The wave-3 pattern observed in panel b.2 is rotated by half a wavelength from the average position of the mean wave-3 pattern associated with Raphael (2004)'s ZW3 index, whose reference locations are marked with points in the figure. Thus, the tropospheric Asymmetric SAM index represents a zonal displacement in the position of the climatological wave-3 pattern.

The amplitude of the first zonal wave numbers at each latitude at 50 hPa and 700 hPa is shown in Figure 8, where wave number zero represents the amplitude of the zonal mean. Zonal wave amplitudes of the spatial pattern described by the Full SAM index (column a) are dominated by the zonal mean (wave-number 0) at both levels. However, zonal waves are important, particularly North of 50°S, with wave-number 1 clearly dominating at 50 hPa (panel a.1) and a more equal mix of waves at 700 hPa (panel a.2). Column b shows that the Asymmetric SAM is overwhelmingly dominated by wave 1 in the stratosphere (panel b.1), while in the troposphere it is composed of zonal waves 3 to 1 in decreasing level of importance (panel b.2) with negligible amplitude of the zonal mean. The Symmetric SAM, on the other hand, it's almost entirely composed of zonal mean at both levels (column c), with little to now contribution from zonal waves with wave-numbers 1 to 3.

We can see that the amplitude and latitudinal distribution zonal waves in the Asymmetric SAM on one hand, and the zonal mean in the Symmetric SAM on the other correspond almost exactly to

the amplitude and latitudinal distribution in the Full SAM. This confirms the correct decomposition of the SAM in its symmetric and asymmetric components. Looking at panel b.2 from Figure 7, it becomes apparent that zonal waves 1 and 2 modulate the amplitude of zonal wave 3, which – as mentioned before – is larger in the Western Hemisphere than in the Eastern Hemisphere.

To analyse the vertical structure of the geopotential height anomalies associated with the asymmetric SAM index, we show a vertical cross section of regressions of mean geopotential height between 65°S and 40°S for the 50 hPa Asymmetric SAM index (panel a) and for the 700 hPa Asymmetric SAM index (panel b) (Figure 9). The geopotential height anomalies associated with the stratospheric Asymmetric SAM (panel a) are clearly constrained to the stratosphere, which underscores the uncoupling between the stratospheric and tropospheric Asymmetric SAM. The vertical structure of this signal tilts about 60° to the West between 100 hPa and 1 hPa, suggesting baroclinic processes. Interestingly, the signal in the stratosphere maximises near 10 hPa despite using the 50 hPa index for the regression.

The tropospheric Asymmetric SAM (panel b) has significant signals that extend upwards to the uppermost levels of the reanalysis. In the troposphere, the wave-3 structure is equivalent barotropic with maximum amplitude at roughly 250 hPa. The anomalies are much more intense in the Western hemisphere, where they extend into the stratosphere. In the Eastern hemisphere the wave-3 signal is weaker and confined to the troposphere while negative anomalies dominate in the stratosphere. So, while the tropospheric Asymmetric SAM index is associated with stratospheric geopotential anomalies, these do not project strongly onto the stratospheric Asymmetric SAM. The structures shown in panels a and b in Figure 9 are robust to the choice of index level. For any stratospheric (above 100 hPa) index, the resulting anomalies are very similar to the wave-1 structure with maximum near 10 hPa in panel a. Conversely, for any tropospheric (below 100 hPa) index, the result is very similar to panel b. The patterns mainly change in amplitude (not shown).

315 The wave-3 pattern from Figure 7 panel b.2 is very similar to the Pacific-South American Pattern
 316 (Mo and Ghil 1987; Kidson 1988) which is a teleconnection pattern associated with the ENSO
 317 (Karoly 1989). Indeed, Fogt et al. (2011) showed that there is a significant relationship between
 318 the SAM and the ENSO. The correlation between the Full SAM and the ENSO as measured by
 319 the Oceanic Niño Index (ONI, Bamston et al. 1997) is -0.16 ($p\text{-value} = 2.8 \times 10^{-4}$). Consistent
 320 with Fan (2007), we show that this relationship is captured entirely by the Asymmetric SAM, as
 321 this index has a partial correlation of -0.26 ($p\text{-value} = 6.3 \times 10^{-9}$) with the ONI controlling for the
 322 effect of the Symmetric SAM, whereas the Symmetric SAM's partial correlation with the ONI is
 323 essentially null (0.019 ; $p\text{-value} = 0.67$). We performed the same analysis using the Multivariate
 324 ENSO Index (Wolter and Timlin 2011) and the Southern Oscillation Index (Ropelewski and Jones
 325 1987) to conclude that these results do not depend on the ENSO index used.

326 *c. Surface Impacts*

sec:impacts

327 To see if there are different surface impacts associated with the asymmetric and symmetric SAM
 328 circulation we regress surface temperature and precipitation onto each of the three SAM indices at
 329 700 hPa. As shown in previous sections, the three indices are highly coherent in the troposphere, so
 330 we select this level to represent the tropospheric circulation for consistency with previous studies.

331 Figure 10 shows regression coefficients of each index at 700 hPa with surface temperature for
 332 each trimester. In Summer, positive values of the Full SAM index (panel a.1) are associated
 333 with negative temperature anomalies near Antarctica which are surrounded by a ring of positive
 334 anomalies. The ring is not zonally symmetric, as there are four clear local maximums around
 335 30°W , 120°W , 150°E and 90°E . In the tropics, there are negative anomalies in the equatorial
 336 Pacific, consistent with the negative correlation between SAM and ENSO. Panels b.1 and c.1
 337 show temperature anomalies associated with positive values of the Asymmetric and Symmetric

338 SAM, respectively. Both the local maximums in the ring and the anomalies in the Pacific regions
339 are present mostly on the Asymmetric SAM regression map, while temperature patterns linked
340 to positive Symmetric SAM show a more zonally consistent ring and less relation to the tropics.
341 Noticeable, temperature anomalies in the Indian ocean, South Africa and Australia are strongly
342 related to Asymmetric SAM. This signal is not present in the regression pattern with the Full
343 SAM. Spring (row 4) features similar patterns but of smaller magnitude, with less regions where
344 regressed anomalies have statistical significance.

345 In Autumn and Winter (rows 2 and 3) the positive ring is only present through its local maximums
346 in the regression with the Full SAM. There are also negative anomalies in Southern Australia, and
347 positive anomalies over New Zealand and Southern South America. These patterns are not
348 significant in the sense that there are no areas with p-values below 0.05 when controlling for
349 FDR following Wilks (2016). However, repeating this analysis with 2-meter temperature from
350 ERA5 resulted in similar patterns that were statistically significant (not shown). Moreover, similar
351 features were observed in station measurements by Jones et al. (2019), although using data from
352 1957 to 2016.

353 The pattern of negative anomalies in the pole surrounded by positive anomalies roughly seen
354 in all seasons – although with varying intensity and small-scale details – translates to enhanced
355 meridional temperature gradient maximised in the zero line, which is consistent with the intensi-
356 fication and poleward migration of the westerlies commonly linked to the SAM through thermal
357 wind balance. It's then not surprising to see it more clearly in association with the Symmetric
358 SAM (at least in Summer and Spring).

359 Figure 10 column b can be partially compared with Figure 11 from Fogt et al. (2012). Although
360 they used station data from 1958 to 2001, main features are reproduced here, such as the strong
361 signal in New Zealand and Australia in Summer and Spring.

Regression of the SAM indices with seasonal mean precipitation and 700 hPa geopotential height are shown in Figures 11 and 12 for Australasia and South America respectively. South Africa is not shown because no significant signal was detected there.

In Australia, the annual regression shows that the Full SAM index is positively associated with precipitation in the Southeastern region (Figure 11 panel a.1), which reproduces the results from Gillett et al. (2006). The separation between Asymmetric and Symmetric SAM suggest that this positive anomaly is explained by the Symmetric SAM only in the East coast (panel c.1). Geopotential anomalies associated with this index (black contours) are indicative of easterly flow from the Tasman Sea, which could explain the positive anomalies in precipitation as found by Hendon et al. (2007). The Asymmetric SAM appears related to increased precipitation in the West coast of Southeastern Australia (panel b.2), which could similarly be explained by the anomalous westerly circulation transporting moist air to the continent from the Indian Ocean.

The seasonal-level regressions show statistically significant anomalies only in Spring, when positive Full SAM is associated with positive precipitation anomalies in Eastern Australia (panel a.5). In this trimester the Symmetric SAM seems to be associated with precipitation in a relatively reduced area of the East Coast (panel c.5) while the positive precipitation anomalies related with positive Asymmetric SAM affect all Eastern Australia (panel b.5).

In Summer, positive Full SAM index is associated with positive precipitation anomalies in Western and Eastern Australia, particularly in the North East (panel a.2). The Eastern part being dominated by the relationship with the Symmetric SAM and the Western, by the Asymmetric SAM. In Autumn, the regression with Full SAM shows positive values in the North, similar to Summer, and a broad area of positive values in the North-East to South-West direction. This structure seems to be associated with the Symmetric SAM, while the Northern positive values are associated with the Asymmetric SAM. In Winter we see the same NE to SW aligned anomaly (although with much

reduced amplitude) that is also present only in relation with the Symmetric SAM. None of these regression coefficients are statistically significant at the 95% level. The Spring signal is broadly consistent with Hendon et al. (2007), but whereas Hendon et al. (2007) also detected a strong signal in Summer, panel a.2 shows no statistically significant association (although the coefficients have the consistent sign).

In South America (Figure 12), the annual-level regression shows that positive SAM is associated with statistically significant precipitation decrease in Southeastern South America (SESA) and Southern Chile and non-significant increase in South Brazil, near the South Atlantic Convergence Zone (SACZ) (panel a.1). Panels b.1 and c.1 show a remarkably clean separation between the Asymmetric SAM – associated with the Southeastern South American and Southern Brazilian signals – and the Symmetric SAM – associated with the signal in Southern Chile.

Except Winter, seasonal-level regressions mirror this same pattern. Even if not statistically significant, they all show negative values in Southeastern South America and Southern Chile along with positive values in Southern Brazil in relation with the Full SAM. The separation of these features between the Asymmetric SAM and Symmetric SAM regression maps is also rather consistent.

The anomalous circulation at 700 hPa associated with the Symmetric SAM (panel c.1) indicate anomalous Easterly flow over Southern Chile. This leads to reduced influx of moist air from the Pacific Ocean which, is the main source of precipitable water in that region (Garreaud 2007). On the other hand, the anomalous circulation associated with positive values of Asymmetric SAM (panel b.1) in the Atlantic is anticyclonic in the South and cyclonic in the North. This creates anomalous South-Easterly flow over Southeastern South America, which inhibits the flow of the Low Level Jet to the region (Silvestri and Vera 2009; Zamboni et al. 2010). This same pattern was found to be associated with increased precipitation in Southern Brazil during South Atlantic

410 Convergence Zone events (Rosso et al. 2018). There is a small area of increased precipitation with
411 SAM near central Argentina which is also present in the station-based analysis by Gillett et al.
412 (2006) and that is explained by the Asymmetric SAM.

413 *d. Conclusions*

414 In this study we characterise the temporal and spatial variability of the zonally symmetric and
415 asymmetric structure of the SAM. By projecting monthly geopotential fields at each level with
416 the corresponding asymmetric and symmetric pattern, we created two indices for representing the
417 zonally asymmetric and symmetric contributions of the SAM respectively.

418 As expected, the Asymmetric SAM index correlates strongly with the Symmetric SAM index.
419 In the troposphere, this correlation is maximum at zero lag, while in the stratosphere is maximised
420 with the Asymmetric SAM leading the Symmetric SAM by one month. Since most indices of the
421 SAM are calculated using surface or near-surface conditions, this result would suggest that they
422 might not be sensitive to the most dramatic changes in SAM variability.

423 The two-year periodicity we found in the stratospheric Symmetric SAM might point to a link
424 between the SAM and the Quasi Biennial Oscillation. There is evidence of influence between the
425 QBO and the Northern Annular Mode (e.g. Holton and Tan 1980; Watson and Gray 2014; Zhang
426 et al. 2020), so it's not unlikely that the SAM would be similarly connected. However establishing
427 this link would require further research.

428 We observe a positive trend towards positive SAM in Summer and Autumn, As was documented
429 by previous studies, such as Fogt and Marshall (2020) (and references therein) for surface levels.
430 We show that these trends are maximised at the 100 hPa level and are explained by the zonally
431 symmetric component. We also find a statistically significant positive trend in the Symmetric
432 component of the SAM in the stratosphere that is not apparent in the Full SAM index. In contrast

433 to Fogt et al. (2012) we find some evidence of the SAM becoming more zonally asymmetric, as
434 there is a slight positive trend in the variance explained by the as the Asymmetric SAM explains
435 an increasingly proportion of the total variance.

436 In the troposphere, the spatial patterns of geopotential associated with the Symmetric SAM are
437 much closer to being truly annular than the patterns associated with the Full SAM index. The
438 Asymmetric SAM, on the other hand, describes a wave-3 pattern with maximum amplitude in
439 the Pacific region and whose phase is rotated a quarter wavelength from the mean zonal wave 3
440 described by Raphael (2004)'s index. This pattern extends in the troposphere but its maximum
441 is located at 250 hPa, which also could suggest that surface-based indices are not optimum for
442 capturing this variability.

443 This wave-3 pattern is similar to the Pacific-South American Pattern, which is a teleconnection
444 pattern linked to ENSO variability. We found that the significant correlation that exists between
445 the Full SAM index and the Oceanic Niño Index is captured entirely by the Asymmetric SAM
446 index. This suggests that ENSO is linked to SAM exclusively through the variability in the latter's
447 asymmetric component and thus, the Asymmetric SAM index could be a useful measure to further
448 study that relationship.

449 Temperature anomalies associated with the Full SAM broadly show a pattern of negative anoma-
450 lies at polar latitudes surrounded by positive anomalies, but with many deviations from symmetry.
451 The Asymmetric SAM index explains a big portion of these deviations. In particular, the positive
452 phase of the Asymmetric SAM is associated with colder temperatures over Southern Brazil, South
453 Africa and Southern Australia, as well as the negative anomalies in the equatorial Pacific consistent
454 with the ENSO-SAM relationship. These negative anomalies are particularly clear in the DJF
455 and SON trimesters, which include the months in which the ENSO teleconnection is more active
456 (Cazes-Boezio et al. 2003; Fogt et al. 2011; Cai et al. 2020).

457 In Australia the Full SAM is associated with positive precipitation anomalies in South East
458 and this is explained by the Symmetric SAM. However, the Asymmetric SAM is associated with
459 a small area of positive precipitation anomalies in the Eastern Coast of West Australia, maybe
460 due to advection of moist air from the Indian Ocean. In South America, precipitation anomalies
461 associated with the Full SAM are negative both in Southern Chile and Southeastern South America,
462 and positive in Southern Brazil. These features are cleanly separated between the Asymmetric and
463 Symmetric components. The Symmetric SAM explains the negative anomalies in Southern Chile
464 and the Asymmetric SAM, the negative-positive dipole between Southeastern South America and
465 Southern Brazil. Individual seasons mostly follow this pattern.

466 Silvestri and Vera (2009) suggests that precipitation impacts linked to the SAM changed rather
467 dramatically before and after 1980. In particular, the negative relationship with precipitation
468 in South America was absent in some areas and switched sign in others in the earlier period.
469 The correlation between ENSO and SAM is similarly non-stationary, also changing sign before
470 the 1980s (Fogt and Bromwich 2006; Clem and Fogt 2013). Seeing as both the ENSO-SAM
471 relationship and most of the precipitation impacts in South America are captured by the Asymmetric
472 SAM, the results presented here are most likely period-dependent.

473 By successfully separating the zonally symmetric and zonally asymmetric SAM signals, we show
474 that the asymmetric component of the SAM has its unique variability, trends and impacts. This
475 is particularly important in the context of a changing climate, as the impact on the SAM of ozone
476 recovery is modeled as highly zonally symmetric, while the impact of increased concentration of
477 greenhouse gases has also a zonally asymmetric component (Arblaster and Meehl 2006; Simpkins
478 and Karpechko 2012).

Acknowledgments. NOAA Global Surface Temperature (NOAAGlobalTemp) data provided by the NOAA/OAR/ESRL PSL, Boulder, Colorado, USA, from their Web site at <https://psl.noaa.gov/>

The research was supported by UBACyT20020170100428BA and the CLIMAX Project funded by Belmont Forum/ANR-15-JCL/-0002-01. Elio Campitelli was supported by a PhD grant from CONICET, Argentina.

Data availability statement. All data used in this paper is freely available in their respective sources. ERA5 data can be obtained via the Copernicus Climate Data Store (<https://cds.climate.copernicus.eu/cdsapp#!/dataset/reanalysis-era5-pressure-levels-monthly-means>). NOAAGlobalTemp and GPCC precipitation data can be obtained through the NOAA Physical Sciences Laboratory website (<https://psl.noaa.gov/data/gridded/data.noaaglobaltemp.html> and <https://psl.noaa.gov/data/gridded/data.gpcc.html>). The Oceanic Niño Index is available via NOAA's Climate Prediction Center: https://www.cpc.ncep.noaa.gov/products/analysis_monitoring/ensostuff/detrend.nino34.ascii.txt

A version-controlled repository of the code used to create this analysis, including the code used to download the data can be found at <https://github.com/eliocamp/asymsam>.

References

Albers, S., and E. Campitelli, 2020: Rsoi: Import Various Northern and Southern Hemisphere Climate Indices.

Allaire, J., J. Horner, Y. Xie, V. Marti, and N. Porte, 2019: *Markdown: Render Markdown with the c Library 'Sundown'*.

Arblaster, J. M., and G. A. Meehl, 2006: Contributions of External Forcings to Southern Annular Mode Trends. *J. Climate*, **19** (12), 2896–2905, doi:10.1175/JCLI3774.1.

501 Baldwin, M. P., 2001: Annular modes in global daily surface pressure. *Geophysical Research*
502 *Letters*, **28** (21), 4115–4118, doi:10.1029/2001GL013564.

503 Baldwin, M. P., and T. J. Dunkerton, 2001: Stratospheric Harbingers of Anomalous Weather
504 Regimes. *Science*, **294** (5542), 581–584, doi:10.1126/science.1063315.

505 Baldwin, M. P., and D. W. J. Thompson, 2009: A critical comparison of stratosphere–troposphere
506 coupling indices. *Quarterly Journal of the Royal Meteorological Society*, **135** (644), 1661–1672,
507 doi:10.1002/qj.479.

508 Baldwin, M. P., and Coauthors, 2001: The quasi-biennial oscillation. *Reviews of Geophysics*,
509 **39** (2), 179–229, doi:10.1029/1999RG000073.

510 Bamston, A. G., M. Chelliah, and S. B. Goldenberg, 1997: Documentation of a highly ENSO-
511 related sst region in the equatorial pacific: Research note. *Atmosphere-Ocean*, **35** (3), 367–383,
512 doi:10.1080/07055900.1997.9649597.

513 Benjamini, Y., and Y. Hochberg, 1995: Controlling the False Discovery Rate: A Practical and
514 Powerful Approach to Multiple Testing. *Journal of the Royal Statistical Society: Series B*
515 *(Methodological)*, **57** (1), 289–300, doi:10.1111/j.2517-6161.1995.tb02031.x.

516 Cai, W., and Coauthors, 2020: Climate impacts of the El Niño–Southern Oscillation on
517 South America. *Nature Reviews Earth & Environment*, **1** (4), 215–231, doi:10.1038/
518 s43017-020-0040-3.

519 Campitelli, E., 2020: metR: Tools for Easier Analysis of Meteorological Fields.

520 Cazes-Boezio, G., A. W. Robertson, and C. R. Mechoso, 2003: Seasonal Dependence of ENSO
521 Teleconnections over South America and Relationships with Precipitation in Uruguay. *J. Climate*,
522 **16** (8), 1159–1176, doi:10.1175/1520-0442(2003)16<1159:SDOETO>2.0.CO;2.

523 Chung, C., and S. Nigam, 1999: Weighting of geophysical data in Principal Component
 524 Analysis. *Journal of Geophysical Research: Atmospheres*, **104 (D14)**, 16 925–16 928, doi:
 525 10.1029/1999JD900234.

526 Clem, K. R., and R. L. Fogt, 2013: Varying roles of ENSO and SAM on the Antarctic Peninsula
 527 climate in austral spring. *Journal of Geophysical Research: Atmospheres*, **118 (20)**, 11,481–
 528 11,492, doi:10.1002/jgrd.50860.

529 Dowle, M., and Coauthors, 2020: Data.table: Extension of 'data.frame'.

530 Fan, K., 2007: Zonal asymmetry of the Antarctic Oscillation. *Geophysical Research Letters*, **34 (2)**,
 531 doi:10.1029/2006GL028045.

532 Fogt, R. L., and D. H. Bromwich, 2006: Decadal Variability of the ENSO Teleconnection to the
 533 High-Latitude South Pacific Governed by Coupling with the Southern Annular Mode. *J. Climate*,
 534 **19 (6)**, 979–997, doi:10.1175/JCLI3671.1.

535 Fogt, R. L., D. H. Bromwich, and K. M. Hines, 2011: Understanding the SAM influ-
 536 ence on the South Pacific ENSO teleconnection. *Clim Dyn*, **36 (7)**, 1555–1576, doi:
 537 10.1007/s00382-010-0905-0.

538 Fogt, R. L., J. M. Jones, and J. Renwick, 2012: Seasonal Zonal Asymmetries in the Southern
 539 Annular Mode and Their Impact on Regional Temperature Anomalies. *J. Climate*, **25 (18)**,
 540 6253–6270, doi:10.1175/JCLI-D-11-00474.1.

541 Fogt, R. L., and G. J. Marshall, 2020: The Southern Annular Mode: Variability, trends, and
 542 climate impacts across the Southern Hemisphere. *WIREs Climate Change*, **11 (4)**, e652, doi:
 543 10.1002/wcc.652.

- 544 Garreaud, R., 2007: Precipitation and Circulation Covariability in the Extratropics. *J. Climate*,
545 **20 (18)**, 4789–4797, doi:10.1175/JCLI4257.1.
- 546 Gillett, N. P., R. J. Allan, and T. J. Ansell, 2005: Detection of external influence on sea level
547 pressure with a multi-model ensemble. *Geophysical Research Letters*, **32 (19)**, doi:10.1029/
548 2005GL023640.
- 549 Gillett, N. P., J. C. Fyfe, and D. E. Parker, 2013: Attribution of observed sea level pressure trends to
550 greenhouse gas, aerosol, and ozone changes. *Geophysical Research Letters*, **40 (10)**, 2302–2306,
551 doi:10.1002/grl.50500.
- 552 Gillett, N. P., T. D. Kell, and P. D. Jones, 2006: Regional climate impacts of the Southern Annular
553 Mode. *Geophysical Research Letters*, **33 (23)**, doi:10.1029/2006GL027721.
- 554 Gong, D., and S. Wang, 1999: Definition of Antarctic Oscillation index. *Geophysical Research*
555 *Letters*, **26 (4)**, 459–462, doi:10.1029/1999GL900003.
- 556 Hendon, H. H., D. W. J. Thompson, and M. C. Wheeler, 2007: Australian Rainfall and Surface
557 Temperature Variations Associated with the Southern Hemisphere Annular Mode. *J. Climate*,
558 **20 (11)**, 2452–2467, doi:10.1175/JCLI4134.1.
- 559 Hersbach, H., and Coauthors, 2020: The ERA5 global reanalysis. *Quarterly Journal of the Royal*
560 *Meteorological Society*, **146 (730)**, 1999–2049, doi:10.1002/qj.3803.
- 561 Ho, M., A. S. Kiem, and D. C. Verdon-Kidd, 2012: The Southern Annular Mode: A comparison of
562 indices. *Hydrology and Earth System Sciences*, **16 (3)**, 967–982, doi:10.5194/hess-16-967-2012.
- 563 Holton, J. R., and H.-C. Tan, 1980: The Influence of the Equatorial Quasi-Biennial Os-
564 cillation on the Global Circulation at 50 mb. *J. Atmos. Sci.*, **37 (10)**, 2200–2208, doi:
565 10.1175/1520-0469(1980)037<2200:TIOTEQ>2.0.CO;2.

566 Hufkens, K., R. Stauffer, and E. Campitelli, 2020: Ecmwfr: Interface to 'ECMWF' and 'CDS'
567 Data Web Services.

568 Jones, J. M., R. L. Fogt, M. Widmann, G. J. Marshall, P. D. Jones, and M. Visbeck, 2009: Historical
569 SAM Variability. Part I: Century-Length Seasonal Reconstructions. *J. Climate*, **22** (20), 5319–
570 5345, doi:10.1175/2009JCLI2785.1.

571 Jones, M. E., D. H. Bromwich, J. P. Nicolas, J. Carrasco, E. Plavcová, X. Zou, and S.-H. Wang, 2019:
572 Sixty Years of Widespread Warming in the Southern Middle and High Latitudes (1957–2016).
573 *J. Climate*, **32** (20), 6875–6898, doi:10.1175/JCLI-D-18-0565.1.

574 Karoly, D. J., 1989: Southern Hemisphere Circulation Features Associated with El Niño-Southern
575 Oscillation Events. *J. Climate*, **2** (11), 1239–1252, doi:10.1175/1520-0442(1989)002<1239:
576 SHCFAW>2.0.CO;2.

577 Katz, R. W., and B. G. Brown, 1991: The problem of multiplicity in research on teleconnections.
578 *International Journal of Climatology*, **11** (5), 505–513, doi:10.1002/joc.3370110504.

579 Kidson, J. W., 1988: Interannual Variations in the Southern Hemisphere Circulation. *J. Climate*,
580 **1** (12), 1177–1198, doi:10.1175/1520-0442(1988)001<1177:IVITSH>2.0.CO;2.

581 Lim, E.-P., H. H. Hendon, J. M. Arblaster, F. Delage, H. Nguyen, S.-K. Min, and M. C. Wheeler,
582 2016: The impact of the Southern Annular Mode on future changes in Southern Hemisphere
583 rainfall. *Geophysical Research Letters*, **43** (13), 7160–7167, doi:10.1002/2016GL069453.

584 Marshall, G. J., 2003: Trends in the Southern Annular Mode from Observations and Reanalyses.
585 *J. Climate*, **16** (24), 4134–4143, doi:10.1175/1520-0442(2003)016<4134:TITSAM>2.0.CO;2.

586 Marshall, G. J., P. A. Stott, J. Turner, W. M. Connolley, J. C. King, and T. A. Lachlan-Cope, 2004:
 587 Causes of exceptional atmospheric circulation changes in the Southern Hemisphere. *Geophysical*
 588 *Research Letters*, **31 (14)**, doi:10.1029/2004GL019952.

589 Mo, K. C., and M. Ghil, 1987: Statistics and Dynamics of Persistent Anomalies. *J. Atmos. Sci.*,
 590 **44 (5)**, 877–902, doi:10.1175/1520-0469(1987)044<0877:SADOPA>2.0.CO;2.

591 R Core Team, 2020: *R: A Language and Environment for Statistical Computing*. Vienna, Austria,
 592 R Foundation for Statistical Computing.

593 Raphael, M. N., 2004: A zonal wave 3 index for the Southern Hemisphere. *Geophysical Research*
 594 *Letters*, **31 (23)**, doi:10.1029/2004GL020365.

595 Rogers, J. C., and H. van Loon, 1982: Spatial Variability of Sea Level Pressure and 500 mb
 596 Height Anomalies over the Southern Hemisphere. *Mon. Wea. Rev.*, **110 (10)**, 1375–1392, doi:
 597 10.1175/1520-0493(1982)110<1375:SVOSLP>2.0.CO;2.

598 Ropelewski, C. F., and P. D. Jones, 1987: An Extension of the Tahiti–Darwin Southern Oscil-
 599 lation Index. *Mon. Wea. Rev.*, **115 (9)**, 2161–2165, doi:10.1175/1520-0493(1987)115<2161:
 600 AEOTTS>2.0.CO;2.

601 Rosso, F. V., N. T. Boiaski, S. E. T. Ferraz, and T. C. Robles, 2018: Influence of the Antarctic
 602 Oscillation on the South Atlantic Convergence Zone. *Atmosphere*, **9 (11)**, 431, doi:10.3390/
 603 atmos9110431.

604 Schneider, U., A. Becker, P. Finger, A. Meyer-Christoffer, B. Rudolf, and M. Ziese, 2015: GPCC
 605 Full Data Reanalysis Version 7.0 at 0.5°: Monthly Land-Surface Precipitation from Rain-Gauges
 606 built on GTS-based and Historic Data: Gridded Monthly Totals. Global Precipitation Clima-

tology Centre (GPCC) at Deutscher Wetterdienst, 20 - 270 MB per decadal gzip compressed NetCDF archive pp., doi:10.5676/DWD_GPCC/FD_M_V7_050.

Schneider, U., P. Finger, A. Meyer-Christoffer, E. Rustemeier, M. Ziese, and A. Becker, 2017: Evaluating the Hydrological Cycle over Land Using the Newly-Corrected Precipitation Climatology from the Global Precipitation Climatology Centre (GPCC). *Atmosphere*, **8** (3), 52, doi:10.3390/atmos8030052.

Sheather, S. J., and M. C. Jones, 1991: A Reliable Data-Based Bandwidth Selection Method for Kernel Density Estimation. *Journal of the Royal Statistical Society. Series B (Methodological)*, **53** (3), 683–690.

Silvestri, G., and C. Vera, 2009: Nonstationary Impacts of the Southern Annular Mode on Southern Hemisphere Climate. *J. Climate*, **22** (22), 6142–6148, doi:10.1175/2009JCLI3036.1.

Simpkins, G. R., and A. Y. Karpechko, 2012: Sensitivity of the southern annular mode to greenhouse gas emission scenarios. *Clim Dyn*, **38** (3), 563–572, doi:10.1007/s00382-011-1121-2.

Smith, T. M., R. W. Reynolds, T. C. Peterson, and J. Lawrimore, 2008: Improvements to NOAA’s Historical Merged Land–Ocean Surface Temperature Analysis (1880–2006). *J. Climate*, **21** (10), 2283–2296, doi:10.1175/2007JCLI2100.1.

Vose, R. S., and Coauthors, 2012: NOAA’s Merged Land–Ocean Surface Temperature Analysis. *Bull. Amer. Meteor. Soc.*, **93** (11), 1677–1685, doi:10.1175/BAMS-D-11-00241.1.

Walker, S. G. T., 1914: *Correlation in Seasonal Variations of Weather, III: On the Criterion for the Reality of Relationships Or Periodicities*. Meteorological Office.

Watson, P. A. G., and L. J. Gray, 2014: How Does the Quasi-Biennial Oscillation Affect the Stratospheric Polar Vortex? *J. Atmos. Sci.*, **71** (1), 391–409, doi:10.1175/JAS-D-13-096.1.

Wickham, H., 2009: *Ggplot2: Elegant Graphics for Data Analysis*. Use R!, Springer-Verlag, New York, doi:10.1007/978-0-387-98141-3.

Wilks, D. S., 2016: “The Stippling Shows Statistically Significant Grid Points”: How Research Results are Routinely Overstated and Overinterpreted, and What to Do about It. *Bull. Amer. Meteor. Soc.*, **97** (12), 2263–2273, doi:10.1175/BAMS-D-15-00267.1.

Wolter, K., and M. S. Timlin, 2011: El Niño/Southern Oscillation behaviour since 1871 as diagnosed in an extended multivariate ENSO index (MEI.ext). *International Journal of Climatology*, **31** (7), 1074–1087, doi:10.1002/joc.2336.

Xie, Y., 2015: *Dynamic Documents with R and Knitr*. 2nd ed., Chapman and Hall/CRC, Boca Raton, Florida.

Zamboni, L., C. R. Mechoso, and F. Kucharski, 2010: Relationships between Upper-Level Circulation over South America and Rainfall over Southeastern South America: A Physical Base for Seasonal Predictions. *J. Climate*, **23** (12), 3300–3315, doi:10.1175/2009JCLI3129.1.

Zhang, R., W. Tian, and T. Wang, 2020: Role of the quasi-biennial oscillation in the downward extension of stratospheric northern annular mode anomalies. *Clim Dyn*, **55** (3), 595–612, doi:10.1007/s00382-020-05285-4.

645

APPENDIX

646

Extra figures

LIST OF FIGURES

Fig. 1.	Spatial patterns of the first EOF of 700 hPa geopotential height for 1979 – 2018 period	34
Fig. 2.	Time series for the Asymmetric SAM and Symmetric SAM indices at (a) 50 hPa and (b) 700 hPa	35
Fig. 3.	Correlation between the Symmetric SAM and Asymmetric SAM index at each level for lag zero and lag -1 (Asymmetric SAM leads Symmetric SAM) for the 1979 – 2018 period	36
Fig. 4.	Cross correlation between levels of the (a) Full SAM, (b) Asymmetric SAM, and (c) Symmetric SAM for the 1979 – 2018 period	37
Fig. 5.	Decadal linear trends at each level for annual (row 1) and seasonal values (rows 2 to 5) for the period 1979 – 2018 and for the (column a) Full SAM index, (column b) Asymmetric SAM index, and (column c) Symmetric SAM index	38
Fig. 6.	Decadal trends of the variance explained by the Asymmetric and Symmetric SAM at each level for the period 1979 – 2018	39
Fig. 7.	Regression of geopotential height (meters) at (row 1) 50 hPa and (row 2) 700 hPa with the (column a) Full SAM, (column b) Asymmetric SAM, and (column c) Symmetric SAM for the 1979 – 2018 period	40
Fig. 8.	Amplitude (meters) of zonal waves of the geopotential height regression patterns in Figure reffig:2d-regr for zonal waves with wave-number 0, 1, 2, and 3, where wave-number 0 represents the amplitude of the zonal mean	41
Fig. 9.	Regression between monthly geopotential height anomalies (meters) averaged between 65° and 40°S and the Asymmetric SAM index (extracted from multiple regression including the Symmetric SAM)	42
Fig. 10.	Regression of seasonal mean surface temperature (Kelvin) with Asymmetric SAM and Symmetric SAM for the 1979 – 2018 period	43
Fig. 11.	Regression of (row 1) annual and (rows 2 to 5) seasonal mean precipitation anomalies (mm per day, shading) and 700 hPa geopotential height (thin lines, positive values as solid lines and negative values as dashed lines) with (column a) Full SAM, (column b) Asymmetric SAM and (column c) Symmetric SAM for the 1979 – 2018 period	44
Fig. 12.	Same as Figure reffig:pp-regr-oceania but for South America	45
Fig. A1.	Lag-correlation between Asymmetric SAM and Symmetric SAM index at each level. Negative lags imply Symmetric SAM leading Asymmetric SAM and vice versa. For the 1979 – 2018 period.	46
Fig. A2.	Fourier spectrum of each timeseries computed as Fourier transform smoothed with modified Daniell smoothers with widths 3 and 5. The shading indicates the 95% confidence area derived by fitting an autoregressive model and computing the spectrum for 5000 simulated samples from the fitted autoregressive model (95% of the simulated samples had an amplitude equal or lower). The light line indicates the theoretical expected amplitude from the autoregressive model. For the 1979 – 2018 period.	47

685	Fig. 13.	50 hPa Geopotetnial height zonal anomalies (meters) of composites of positive and negative	
686		SAM months selected using ± 1 standard deviation as threshold for the 1979 – 2018 period . . .	48
687	Fig. 14.	700 hPa Geopotetnial height zonal anomalies (meters) of composites of positive and negative	
688		SAM months selected using ± 1 standard deviation as threshold for the 1979 – 2018 period . . .	49
689	Fig. 15.	Regression coefficients of 50 hPa and 700 hPa geopotential height zonal anomalies (meters)	
690		onto the standarised timeseries of the leading EOF computed for each season independently	
691		for the 1979 – 2018 period	50
692	Fig. 16.	Regression of 50 hPa and 700 hPa geopotential height zonal anomalies (meters) onto the	
693		standarised timeseries of the leading EOF computed for the periods 1979 – 1998 and 1999	
694		– 2018	51

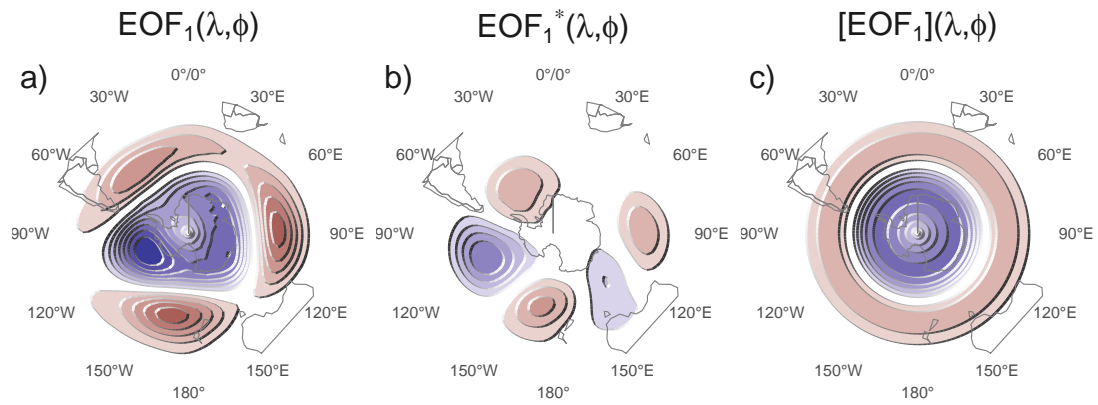


FIG. 1: Spatial patterns of the first EOF of 700 hPa geopotential height for 1979 – 2018 period. (a) Full field, (b) zonally asymmetric component and (c) zonally symmetric component. Arbitrary units.

fig:method

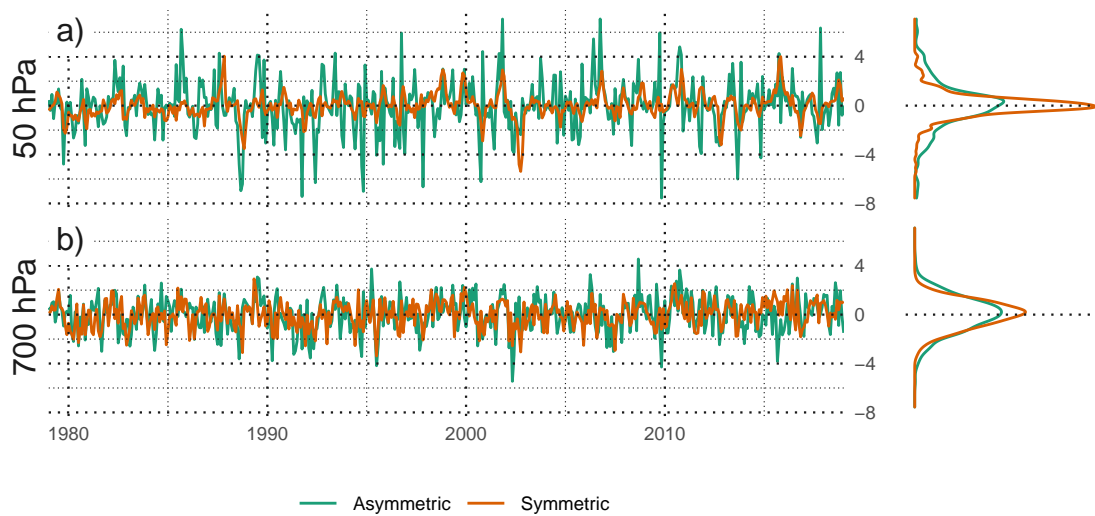


FIG. 2: Time series for the Asymmetric SAM and Symmetric SAM indices at (a) 50 hPa and (b) 700 hPa. To the right, probability density estimate of each index. Series are standardised by the standard deviation of the Full SAM at each level.

fig:asysam-timeseries

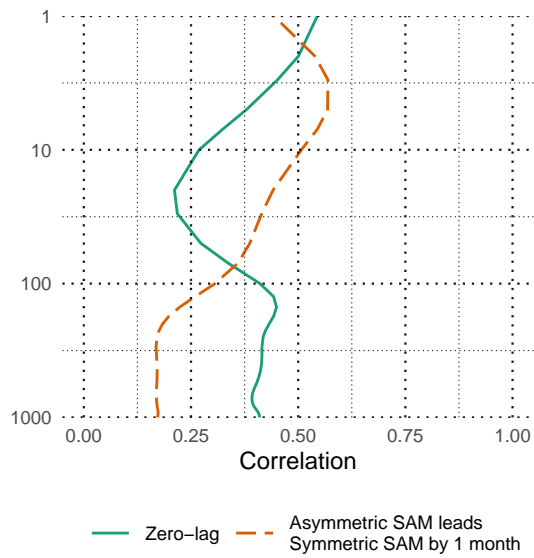


FIG. 3: Correlation between the Symmetric SAM and Asymmetric SAM index at each level for lag zero and lag -1 (Asymmetric SAM leads Symmetric SAM) for the 1979 – 2018 period.

fig:cor-lev

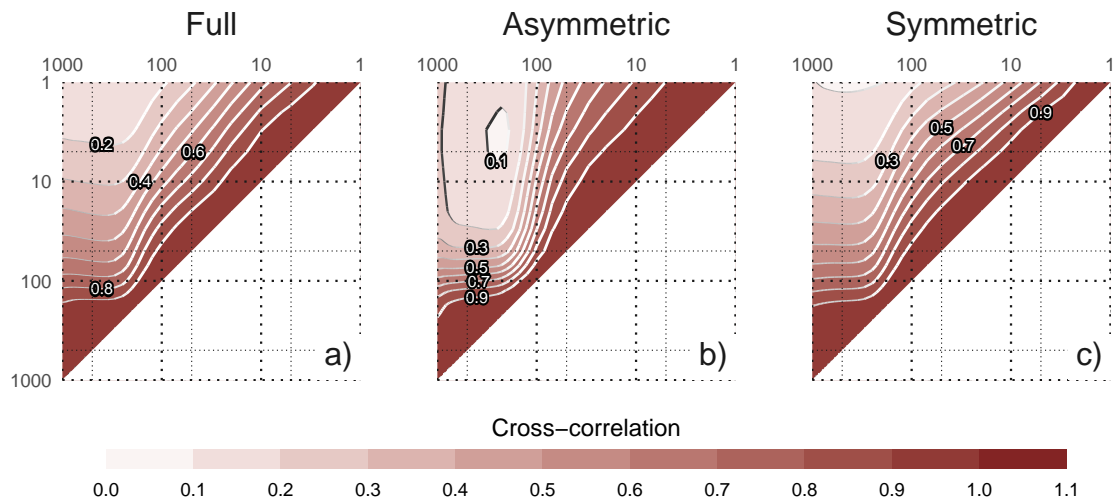


FIG. 4: Cross correlation between levels of the (a) Full SAM, (b) Asymmetric SAM, and (c) Symmetric SAM for the 1979 – 2018 period.

fig:cross-correlation

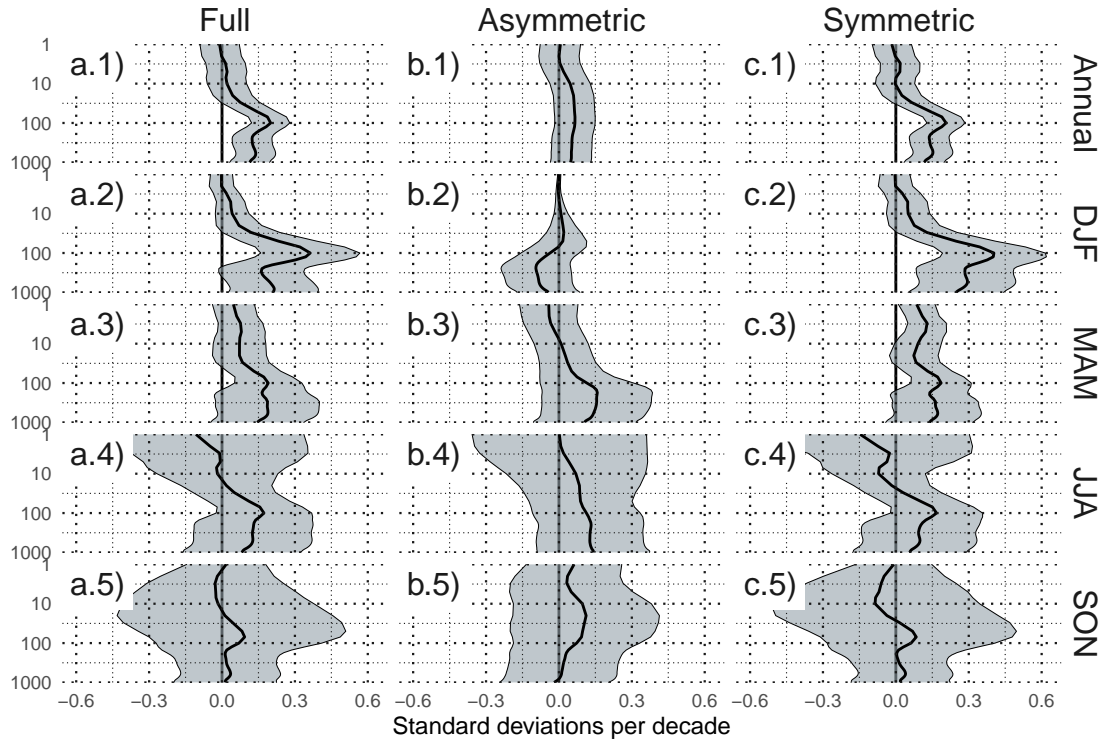


FIG. 5: Decadal linear trends at each level for annual (row 1) and seasonal values (rows 2 to 5) for the period 1979 – 2018 and for the (column a) Full SAM index, (column b) Asymmetric SAM index, and (column c) Symmetric SAM index. Shading indicates the 95% confidence interval from a t-distribution.

fig:trends

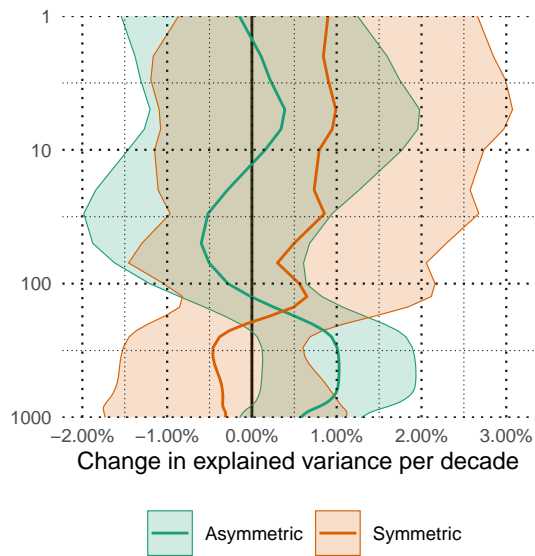


FIG. 6: Decadal trends of the variance explained by the Asymmetric and Symmetric SAM at each level for the period 1979 – 2018. Shading indicates the 95% confidence interval.

fig:r-squared-trend

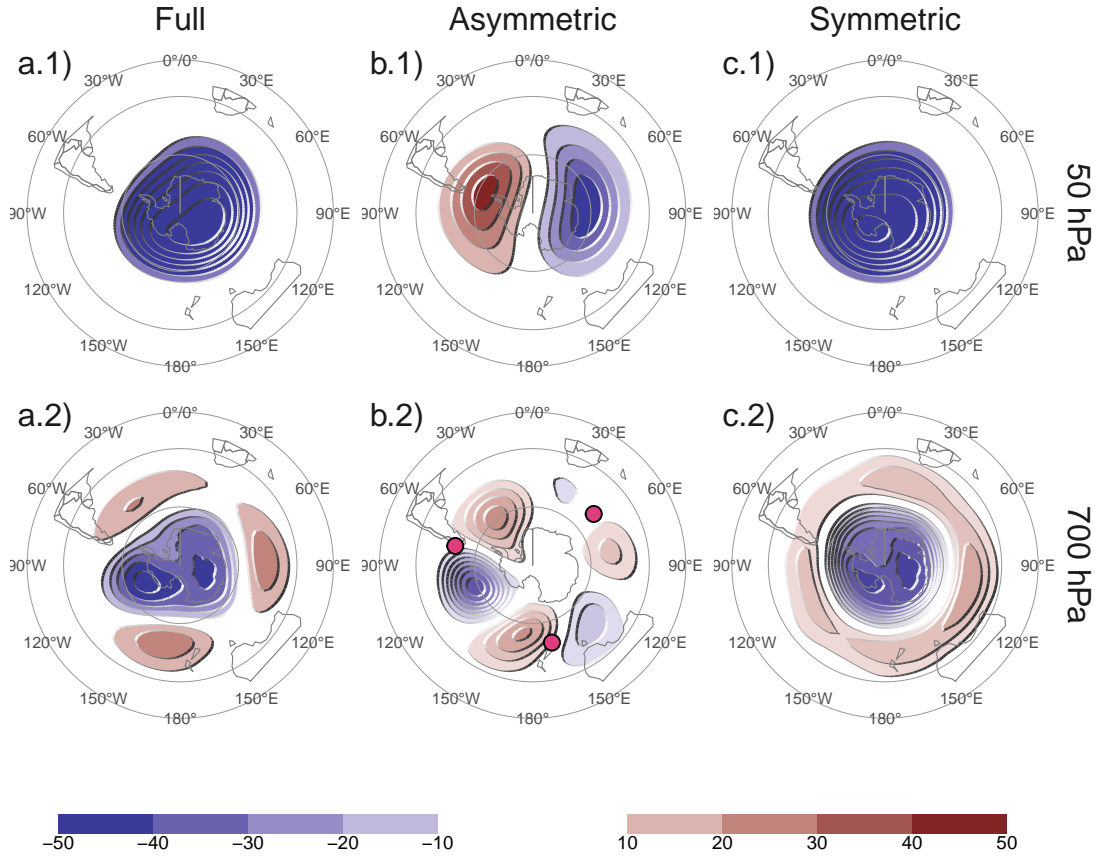


FIG. 7: Regression of geopotential height (meters) at (row 1) 50 hPa and (row 2) 700 hPa with the (column a) Full SAM, (column b) Asymmetric SAM, and (column c) Symmetric SAM for the 1979 – 2018 period. The regression patterns for Asymmetric and Symmetric SAM are the result of one multiple regression using both indices. Points marked on panel b.2 are the location of the reference points used by Raphael (2004) for their Zonal Wave 3 index.

fig:2d-regr

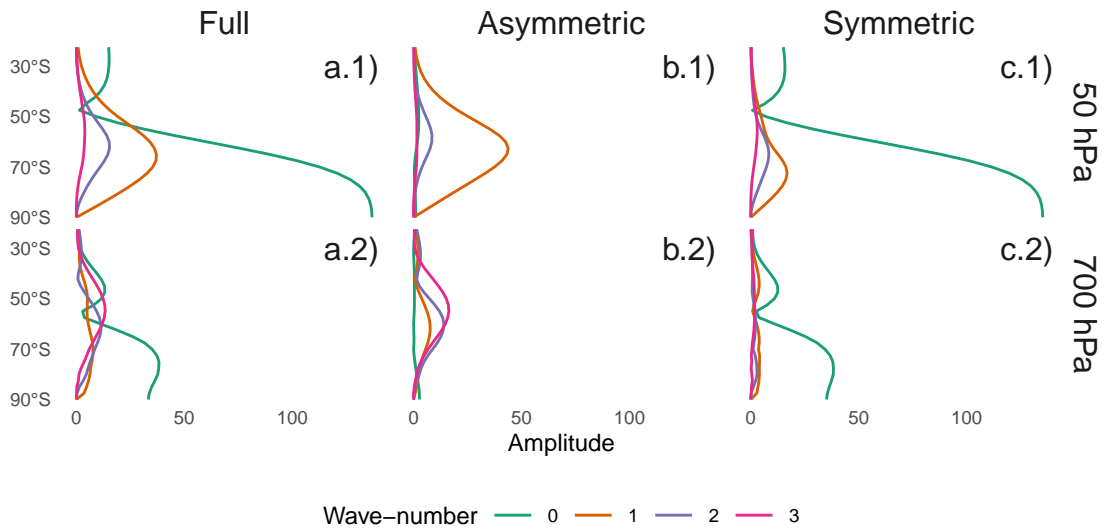


FIG. 8: Amplitude (meters) of zonal waves of the geopotential height regression patterns in Figure reffig:2d-regr for zonal waves with wave-number 0, 1, 2, and 3, where wave-number 0 represents the amplitude of the zonal mean.

fig:wave-amplitude

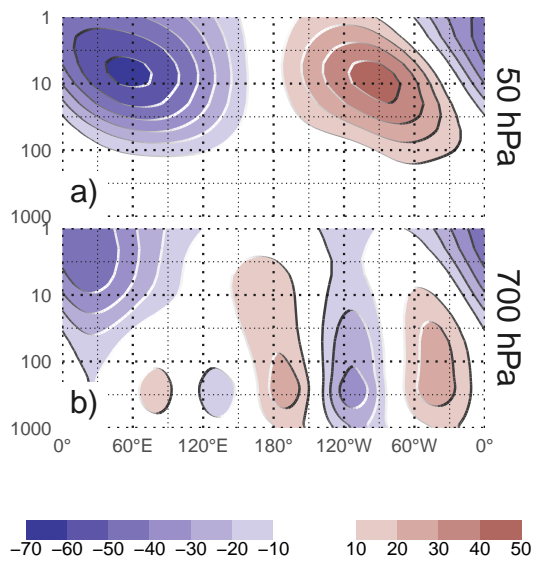


FIG. 9: Regression between monthly geopotential height anomalies (meters) averaged between 65° and 40°S and the Asymmetric SAM index (extracted from multiple regression including the Symmetric SAM). (a) With the Asymmetric SAM in 50 hPa and (b) in 700 hPa for the 1979 – 2018 period.

fig:vertical-regression

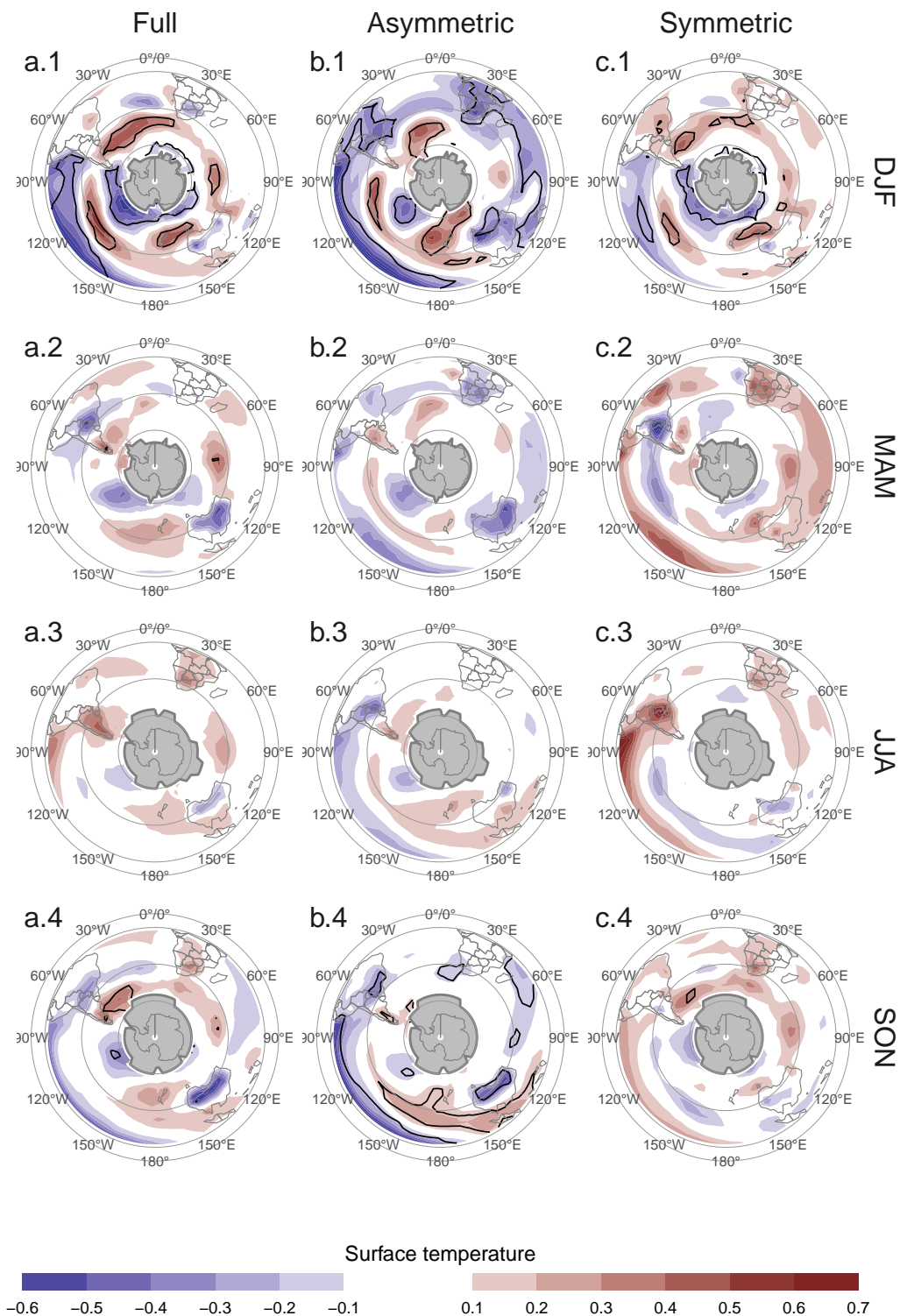


FIG. 10: Regression of seasonal mean surface temperature (Kelvin) with Asymmetric SAM and Symmetric SAM for the 1979 – 2018 period. Black contours indicate areas with p-value smaller than 0.05 controlling for False Detection Rate. Gray areas in Antarctica are areas with have more than 15% of missing data.

fig:regr-air-season

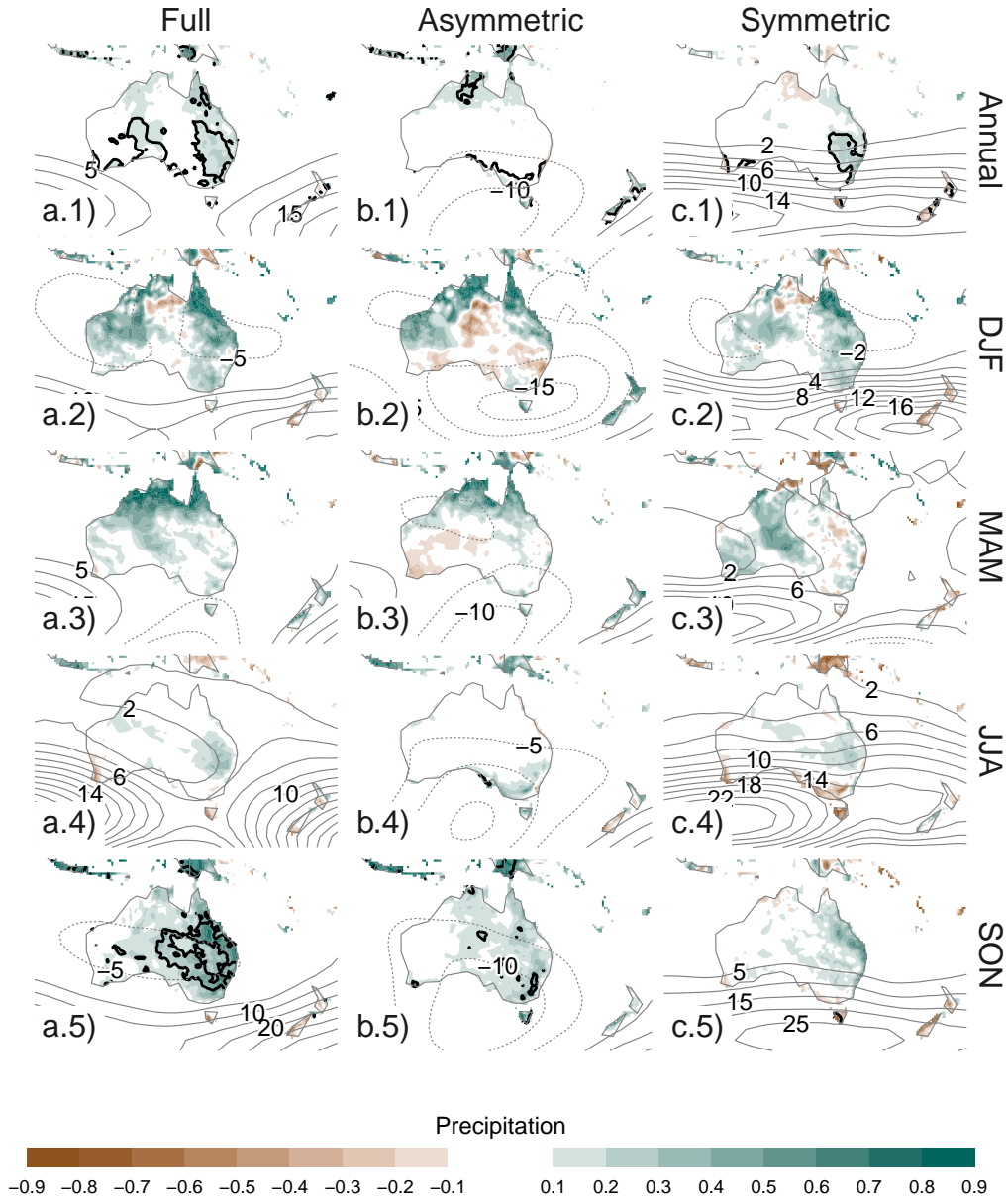


FIG. 11: Regression of (row 1) annual and (rows 2 to 5) seasonal mean precipitation anomalies (mm per day, shading) and 700 hPa geopotential height (thin lines, positive values as solid lines and negative values as dashed lines) with (column a) Full SAM, (column b) Asymmetric SAM and (column c) Symmetric SAM for the 1979 – 2018 period. Thin lines are the Black contours indicate areas with p-value smaller than 0.05 controlling for False Detection Rate.

fig:pp-regr-oceania

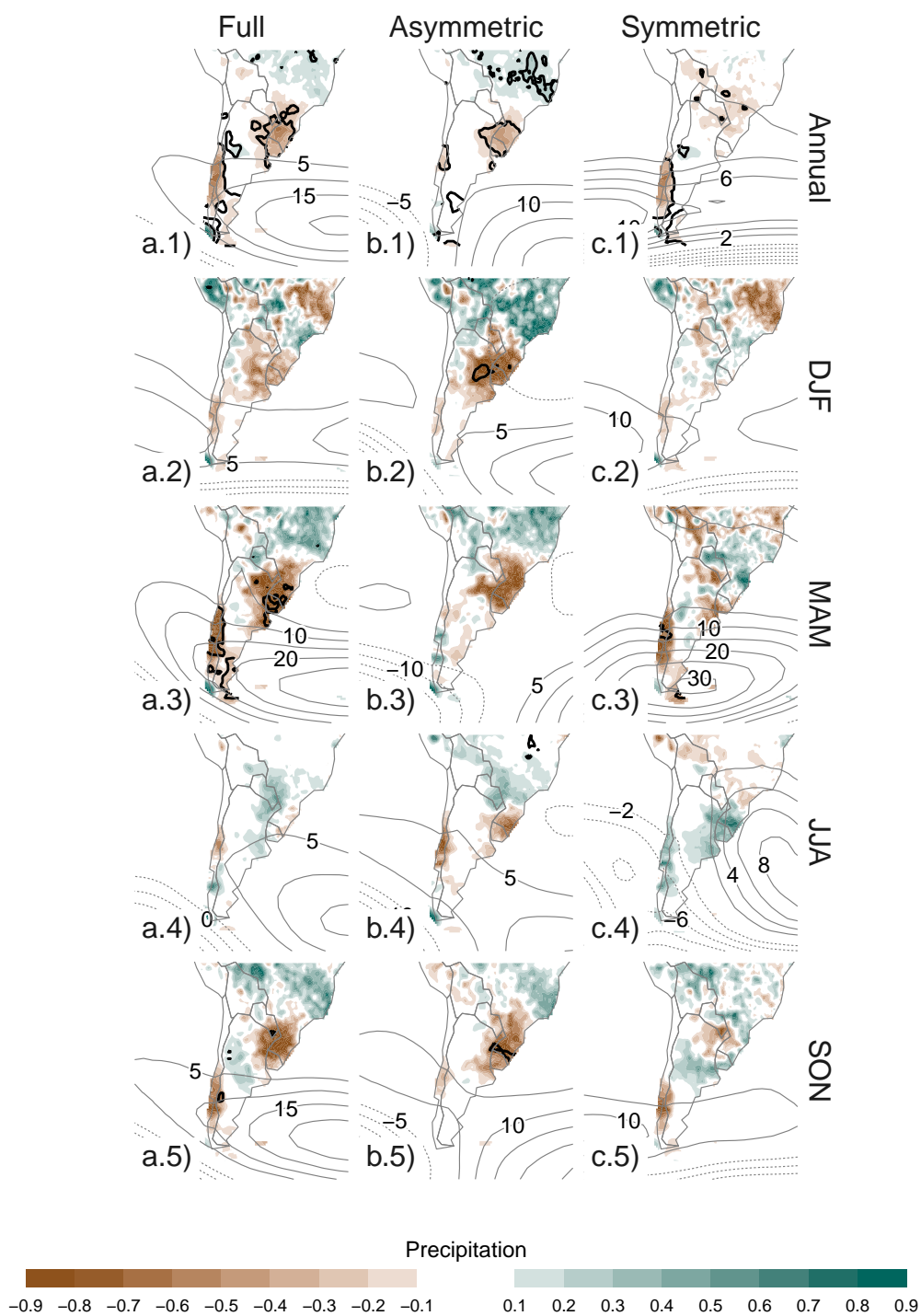


FIG. 12: Same as Figure
refig:pp-regr-oceania but for South America.

fig:pp-regr-america

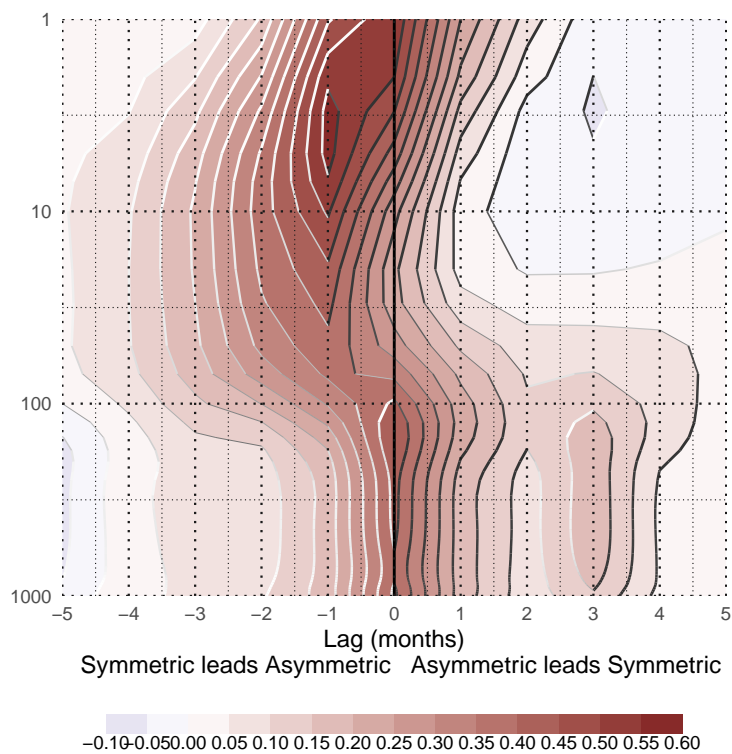


Fig. A1: Lag-correlation between Asymmetric SAM and Symmetric SAM index at each level. Negative lags imply Symmetric SAM leading Asymmetric SAM and vice versa. For the 1979 – 2018 period.

fig:A1

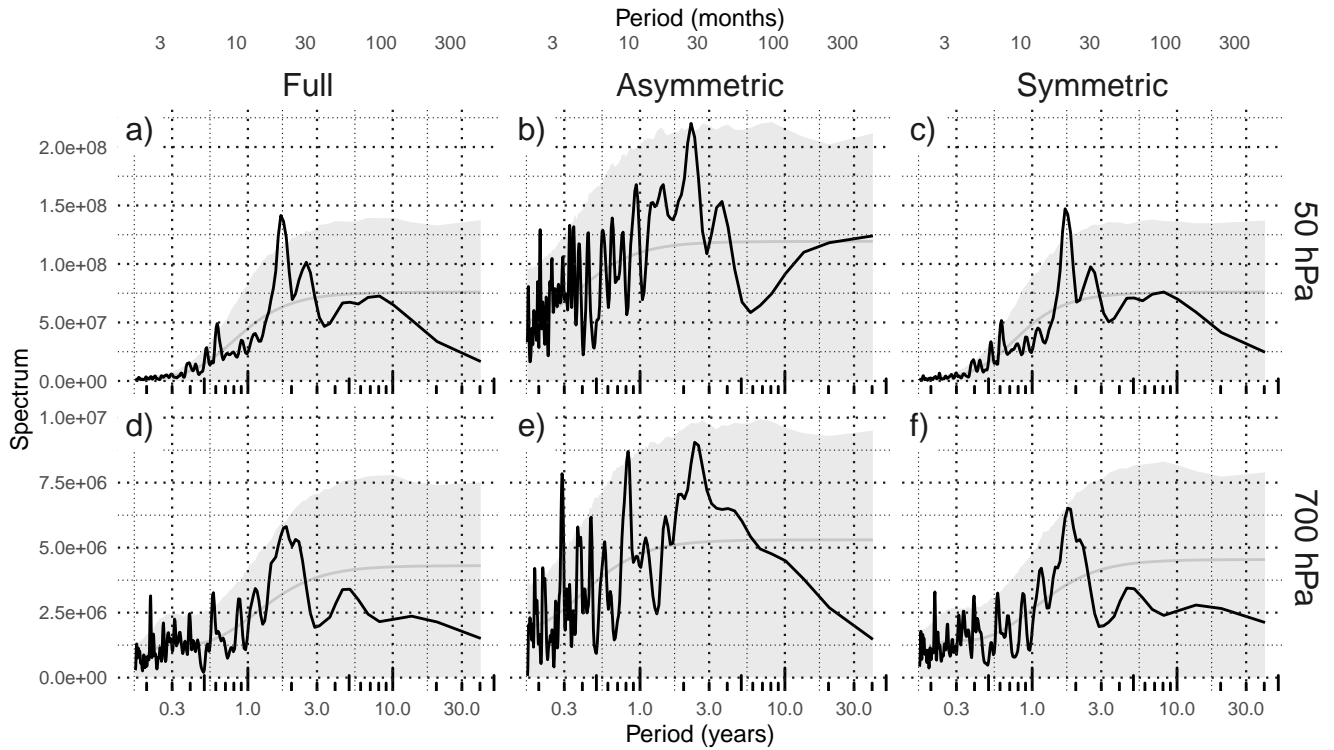


Fig. A2: Fourier spectrum of each timeseries computed as Fourier transform smoothed with modified Daniell smoothers with widths 3 and 5. The shading indicates the 95% confidence area derived by fitting an autoregressive model and computing the spectrum for 5000 simulated samples from the fitted autoregressive model (95% of the simulated samples had an amplitude equal or lower). The light line indicates the theoretical expected amplitude from the autoregressive model. For the 1979 – 2018 period.

fig:A2

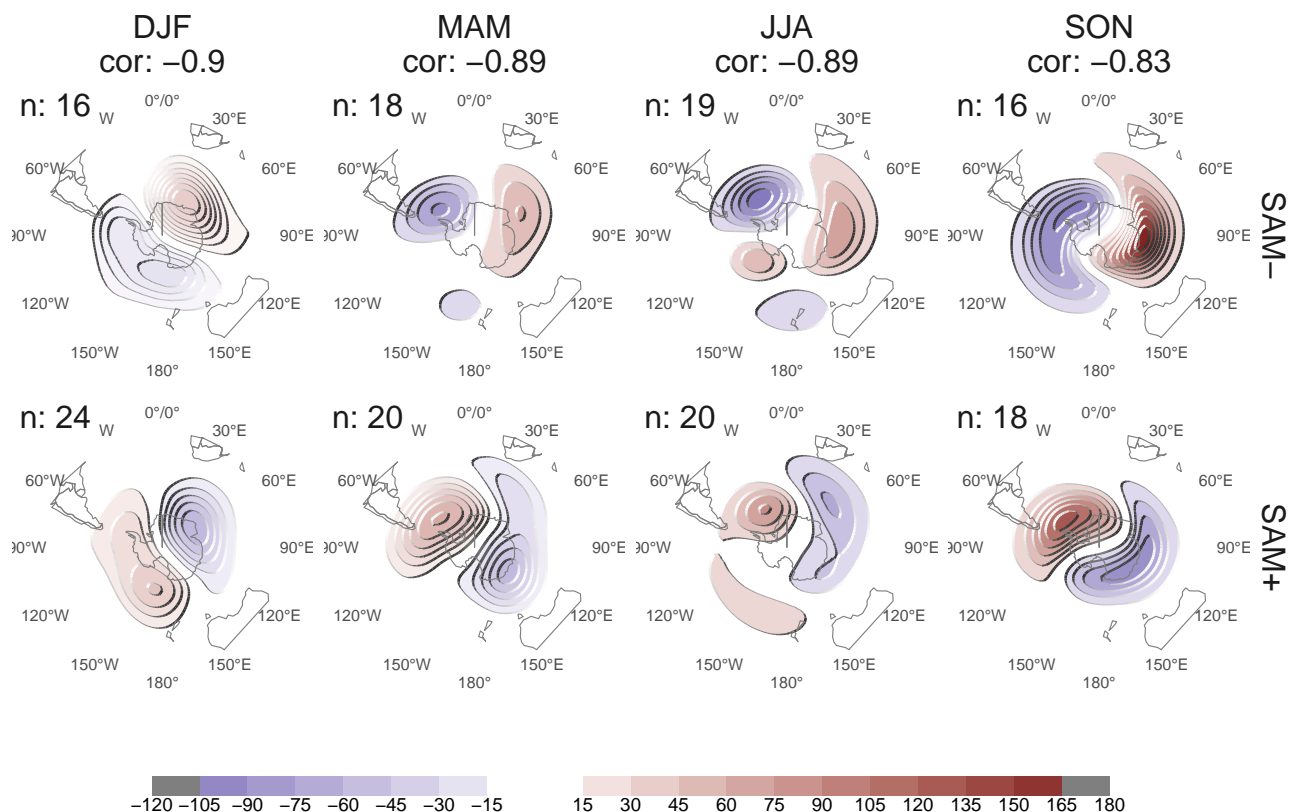


FIG. 13: 50 hPa Geopotential height zonal anomalies (meters) of composites of positive and negative SAM months selected using ± 1 standard deviation as threshold for the 1979 – 2018 period. Numbers in the column headers are pattern correlation between SAM+ and SAM- composites and number of monthly fields used to construct the composites.

fig:A3

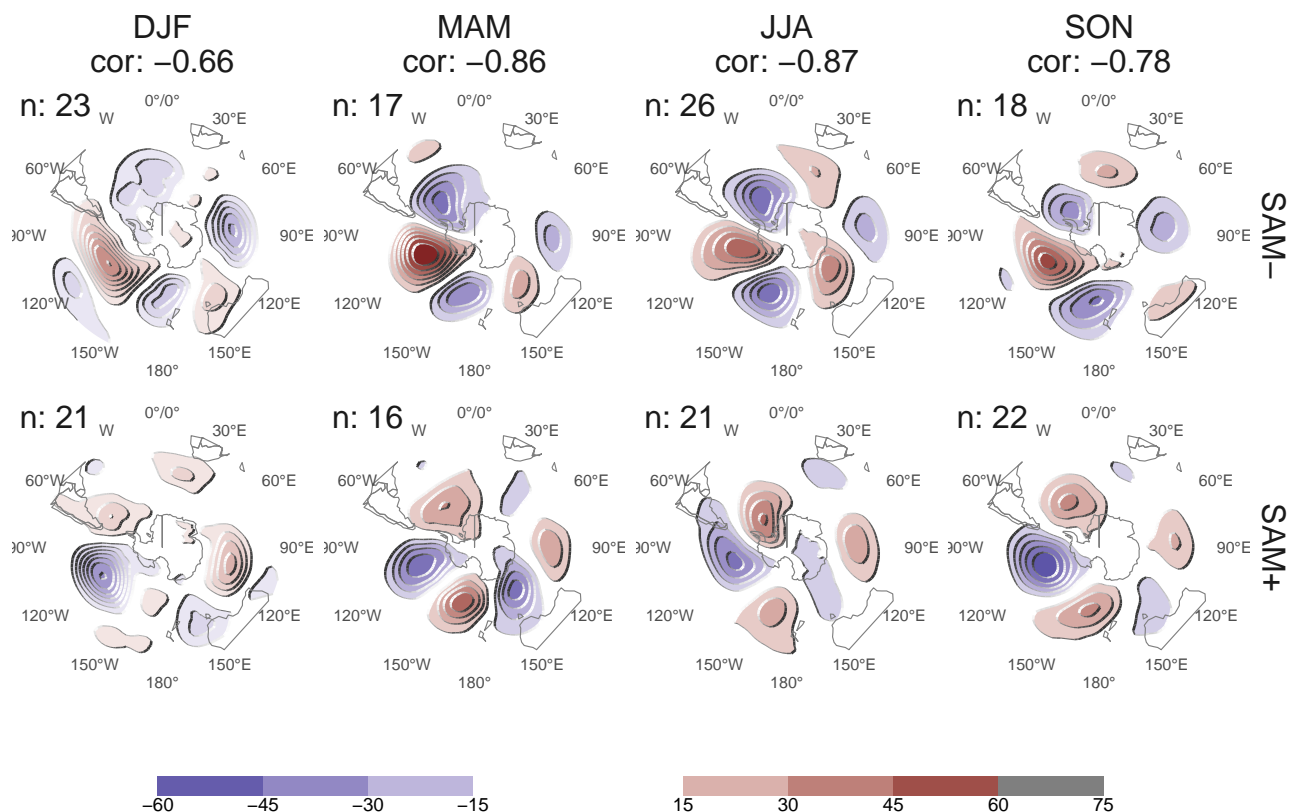


FIG. 14: 700 hPa Geopotential height zonal anomalies (meters) of composites of positive and negative SAM months selected using ± 1 standard deviation as threshold for the 1979 – 2018 period. Numbers in the column headers are pattern correlation between SAM+ and SAM- composites and number of monthly fields used to construct the composites.

fig:A4

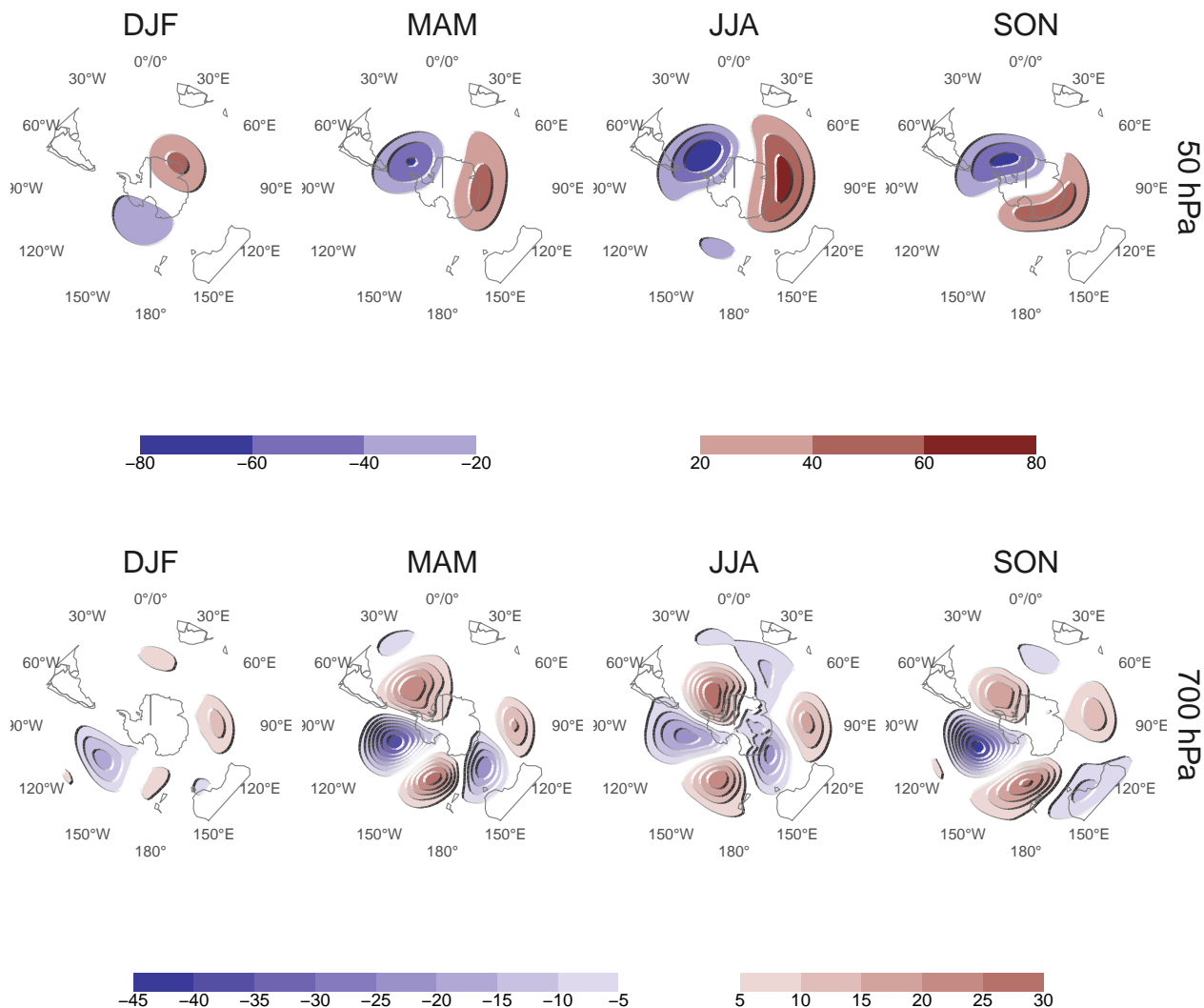


FIG. 15: Regression coefficients of 50 hPa and 700 hPa geopotential height zonal anomalies (meters) onto the standardised timeseries of the leading EOF computed for each season independently for the 1979 – 2018 period.

fig:A5

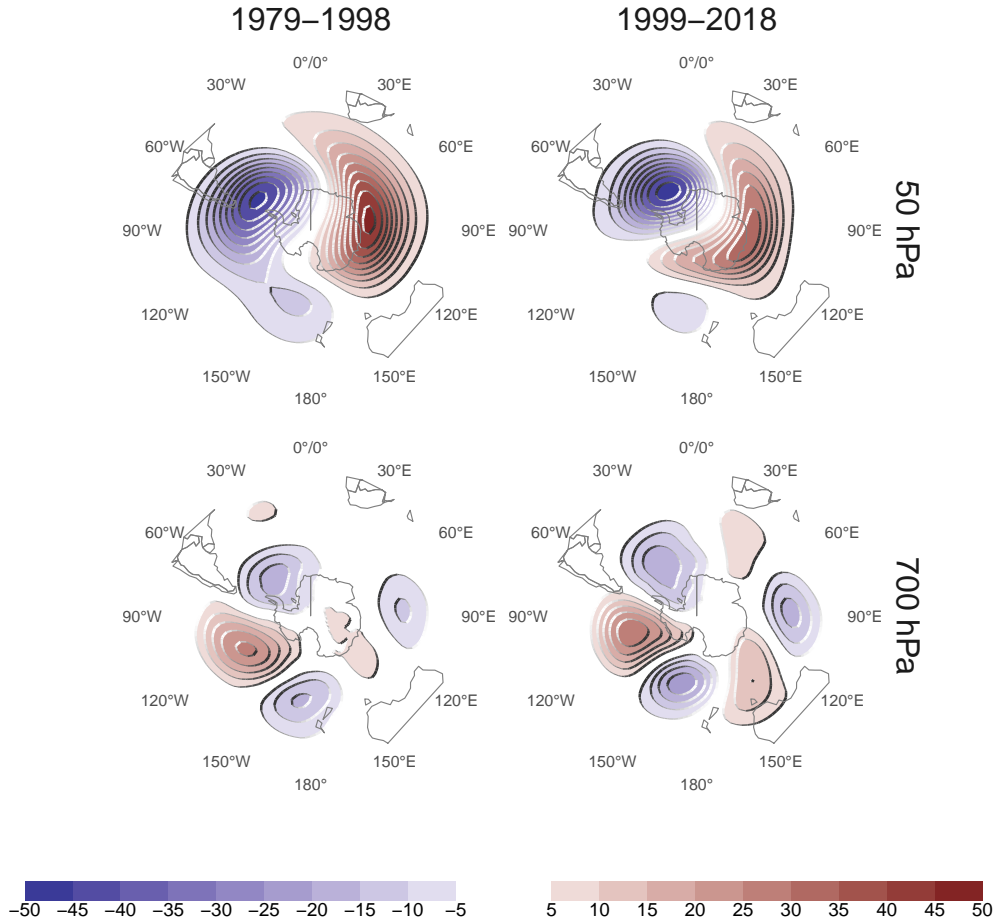


FIG. 16: Regression of 50 hPa and 700 hPa geopotential height zonal anomalies (meters) onto the standardised timeseries of the leading EOF computed for the periods 1979 – 1998 and 1999 – 2018. Pattern correlation between both fields is 0.86 for the 50 hPa fields and 0.76 for the 700 hPa fields.
fig:A6